


Formation and Evolution of Compact Binaries Containing Intermediate Mass Black Holes in Dense Star Clusters

SEUNGJAE LEE ¹, HYUNG MOK LEE ^{2,3}, JI-HOON KIM ^{1,3,4}, RAINER SPURZEM ^{5,6,7}, JONGSUK HONG ⁸ AND
EUNWOO CHUNG ¹

¹*Center for Theoretical Physics, Department of Physics and Astronomy, Seoul National University, Seoul 08826, Korea*

²*Research Institute for Basic Sciences, Seoul National University, Seoul 08826, Korea*

³*Seoul National University Astronomy Research Center, Seoul 08826, Korea*

⁴*Institute for Data Innovation in Science, Seoul National University, Seoul 08826, Korea*

⁵*Astronomisches Rechen-Institut, Zentrum für Astronomie der Universität Heidelberg, Mönchhofstr. 12-14, D-69120 Heidelberg, Germany*

⁶*National Astronomical Observatories and Key Laboratory of Computational Astrophysics, Chinese Academy of Sciences, 20A Datun Rd., Chaoyang District, Beijing 100101, China*

⁷*Kavli Institute for Astronomy and Astrophysics, Peking University, Yiheyuan Lu 5, Haidian Qu, 100871, Beijing, China*

⁸*Korea Astronomy and Space Science Institute, Daejeon 34055, Republic of Korea*

ABSTRACT

We investigate the evolution of star clusters containing intermediate-mass black hole (IMBH) of 300 to $5000 M_{\odot}$, focusing on the formation and evolution of IMBH-stellar mass black holes (SBHs; $M_{\text{BH}} \lesssim 10^2 M_{\odot}$) binaries. Dense stellar systems like globular clusters (GCs) or nuclear star clusters offer unique laboratories for studying the existence and impact of IMBHs. IMBHs residing in GCs have been under speculation for decades, with their broad astrophysical implications for the cluster’s dynamical evolution, stellar population, GW signatures, among others. While existing GW observatories such as the Advanced Laser Interferometer Gravitational-wave Observatory (aLIGO) target binaries with relatively modest mass ratios, $q \lesssim 10$, future observatories such as the Einstein Telescope (ET) and the Laser Interferometer Space Antenna (LISA) will detect intermediate-mass ratio inspirals (IMRIs) with $q > 10$. This work explores the potential for detecting IMRIs adopting these upcoming telescopes. For our experiments, we perform multiple direct N -body simulations with IMBHs utilizing Nbody6++GPU, after implementing the GW merger schemes for IMBHs. We then study the statistical properties of the resulting IMRIs, such as the event rates and orbital properties. Assuming that IMRIs with a signal-to-noise ratio $S/N > 8$ are detectable, we derive the following detection rates for each observatory: $\lesssim 0.02 \text{ yr}^{-1}$ for aLIGO, $\sim 101 - 355 \text{ yr}^{-1}$ for ET, $\sim 186 - 200 \text{ yr}^{-1}$ for LISA, $\sim 0.24 - 0.34 \text{ yr}^{-1}$ for aSOGRO, and $\sim 3880 - 4890 \text{ yr}^{-1}$ for DECIGO. Our result confirms the capability of detecting IMRIs with future GW telescopes.

Keywords: methods: numerical, galaxies: star clusters, galaxies: supermassive black holes, star clusters: general, gravitational waves, black hole physics

1. INTRODUCTION

Commonly classified as intermediate-mass black holes (IMBHs), black holes (BHs) with masses ranging from 10^2 to $10^5 M_{\odot}$, bridge the gap between stellar-mass black holes (SBHs; $M_{\text{BH}} \lesssim 10^2 M_{\odot}$) and the massive black holes (MBHs; $M_{\text{BH}} \gtrsim 10^6 M_{\odot}$), typically found at the galactic centers (for

reviews, see e.g., [Greene et al. 2020](#)). IMBHs may be the key to understanding the origin of MBHs and play critical roles in various astrophysical environments. However, their definitive detection and characterization remain exceptionally challenging due to their relatively modest gravitational influence and the limitations of current observational resolution.

Dense star clusters such as globular clusters (GCs; $M_{\text{GC}} \sim 10^3 - 10^6 M_{\odot}$) and nuclear star clusters (NSCs; $M_{\text{NSC}} \sim 10^6 - 10^8 M_{\odot}$) have long been considered as the possible

Corresponding author: Seungjae Lee, balgun1004@gmail.com

Corresponding author: Ji-hoon Kim, mornkr@snu.ac.kr

habitats for IMBHs. NSCs, the most massive stellar system at galactic centers (for reviews, see e.g., Neumayer et al. 2020), are known for their co-existence with MBHs (e.g., Bacon et al. 1994; Nguyen et al. 2018). Some studies such as Antonini et al. (2015) have proposed that MBHs might be correlated with their host NSCs. A naive generalization of this result leads us to speculate that the IMBHs can be populated in GCs or lower-mass NSCs.

If IMBHs do exist within GCs, there might be multiple possible pathways toward their coexistence. One possibility is that the IMBHs form via frequent dynamical interactions between stars and BHs within dense star clusters like GCs. If the core of a star cluster without a central massive object quickly contracts because of the gravothermal catastrophe (Cohn 1980; Takahashi 1995), it could lead to the formation of a very massive star (VMS) through frequent star-star collisions, eventually collapsing into a BH with a mass above the upper mass gap (Begelman & Rees 1978; Portegies Zwart & McMillan 2002; Gürkan et al. 2004; Freitag et al. 2006c,b; Giersz et al. 2015; Mapelli 2016). Alternatively, a stellar-mass BH might grow through multiple interactions with stars and other stellar-mass BHs (Giersz et al. 2015; Rizzuto et al. 2021; González et al. 2021). Another possibility is that a wandering IMBH is captured by a star cluster and eventually settles in its core.

Although it is very challenging to detect IMBHs with current observation and measurement techniques, there are several IMBH candidates discovered so far (Greene et al. 2020). One example is a luminous X-ray outburst suggested to be a tidal disruption (TD) event induced by IMBH (Lin et al. 2018). Some studies suggest that there can be IMBHs within GCs such as ω Cen (Noyola et al. 2010; Baumgardt 2017). It is recently backed up by the fast-moving stars in the innermost area ($\lesssim 0.08$ pc) of the star cluster (Häberle et al. 2024). Additionally, IMBHs can be populated inside the galactic nuclei of low-mass galaxies (den Brok et al. 2015; Nguyen et al. 2019; Woo et al. 2019) as an extension of galaxy-MBH relation (Kormendy & Ho 2013). However, none of these studies have definitively confirmed the existence of IMBHs.

Conclusive evidence for IMBHs with masses $\gtrsim 10^3 M_\odot$ is still lacking in the gravitational wave (GW) as well. For example, while the GW research has made significant progress in the last few years, most GW signals detected so far have been associated with mergers between BHs with masses $\lesssim 100 M_\odot$. Currently, the main observational targets of existing GW observatories such as Advanced Laser Interferometer Gravitational-wave Observatory (aLIGO) and Virgo, or the upcoming third-generation Einstein Telescope (ET) are binaries with mass ratios $q \lesssim 10$. However, they may be capable of detecting some binaries involving IMBHs — including the intermediate mass ratio inspirals (IMRIs) of mass ratios $q > 10$ (Hild et al. 2011; Sathyaprakash et al. 2012; Amaro-

Seoane 2018). Moreover, the space-based Laser Interferometer Space Antenna (LISA), Decihertz Interferometer Gravitational Wave Observatory (DECIGO), or the Advanced Superconducting Omnidirectional Gravitational Radiation Observatory (aSOGRO; Paik et al. 2016; Bae et al. 2024) will be specialized at detecting lower frequency bands. In addition, those observatories are likely to complement each other due to their distinct detection bands. These GW signatures may prove to be a promising way to establish the existence of IMBHs.

Numerous works made estimates of the IMRI or their detection rates for decades using semi-analytic or numerical framework. The early semi-analytic works prospected that the aLIGO would detect IMRIs including IMBHs with masses $M_{\text{IMBH}} < 350 M_\odot$ in the rate $\lesssim 10 - 30 \text{ yr}^{-1}$ (Brown et al. 2007; Mandel et al. 2008). With a broader IMBH mass range ($\sim 100 - 1000 M_\odot$), the analytic work of Gair et al. (2011) provided the IMRI event rate of $2 - 175 \text{ yr}^{-1}$. Recently, Fragione et al. (2022) proposed that the detection rate of ET would be $0.01 - 10 \text{ Gpc}^{-3} \text{ yr}^{-1}$ for IMBH with masses $\lesssim 1000 M_\odot$. In the side of numerical experiments, Hong & Lee (2015) explored the evolution of NSC in the presence of MBHs with GPU accelerated NBODY6 code (Nitadori & Aarseth 2012), but they mainly focused on the formation of SBH binaries. Arca Sedda et al. (2021) simulated the evolution of three-body systems (one IMBH and two SBHs) within the GC potential. They obtained the IMRI detection rate ranging from 0.003 yr^{-1} to 3000 yr^{-1} which depends on the nature of detectors. Wang et al. (2022) provided the IMRI rates $\sim 0.1 - 0.8 \text{ Gpc}^{-3} \text{ yr}^{-1}$ for IMBH with masses $M_{\text{IMBH}} \lesssim 1000 M_\odot$ in the population III (Pop III) star clusters utilizing a direct N -body simulation code PETAR (Wang et al. 2020).

In this work, we explore the possibility of detecting IMRIs by the existing and upcoming GW observatories by estimating the detection rate of IMRIs in GCs under the assumption of their coexistence. We perform a suite of direct N -body simulations using the code Nbody6++GPU (Kamlah et al. 2022; Spurzem & Kamlah 2023) to study the dynamical interactions of an IMBH embedded at the center of a dense stellar system. Our simulation incorporates the GW merger and TD of the IMBHs, allowing the IMBHs to accrete SBHs and stars nearby. Also, we examine the IMBH mass range ($300 - 5000 M_\odot$) broader than most of the precedent studies as LISA is expected to have advantages in detecting IMRIs including an IMBH with mass $\gtrsim 1000 M_\odot$. Lastly, we investigate the statistics of the resulting GW merger events such as their orbital properties and their detectability by 5 different instruments (aLIGO, ET, LISA, aSOGRO, and DECIGO).

This paper is organized as follows. In Section 2, we briefly describe our code Nbody6++GPU and the IMBH model we have implemented, such as GW merger and TD. Then we

provide the initial conditions tested in our studies in Section 3. We show the result of our simulations including the IMRI rates in Section 4. Finally, we discuss our result in Section 5 and conclude our study in Section 6.

2. METHODS

In this work, we carry out a series of simulations by exploiting the state-of-the-art direct summation N -body simulation code with GPU acceleration, `Nbody6++GPU`. It utilizes a 4th-order Hermite integrator with individual block-time steps and advanced methods for handling close encounters and few-body dynamics (McMillan 1986; Hut et al. 1995). These methods include the Kustaanheimo-Stiefel (KS) regularization (Kustaanheimo et al. 1965), the Ahmad-Cohen scheme for neighboring stars (Ahmad & Cohen 1973), and algorithmic chain regularization (Mikkola & Tanikawa 1999; Mikkola & Merritt 2008). This combination is capable of tracking the detailed evolution of binaries with periods up to 10^{-10} times shorter than the dynamical timescales of star clusters. For details of the methods adopted in `Nbody6++GPU`, we refer the interested readers to Aarseth (1999, 2003), Wang et al. (2015), Kamlah et al. (2022), and Spurzem & Kamlah (2023).

2.1. Prescriptions of Gravitational Wave (GW) Mergers and Tidal Disruptions

This section briefly introduces how the code handles close encounters and then describes how we implement GW mergers and TDs for IMBHs in our simulations. The IMBH embedded in a dense star cluster experiences multiple interactions with stars and BHs. A close encounter between the two particles with masses M_1 and M_2 at a distance R is treated by the KS regularization scheme,¹ provided the following conditions are met:

- the two particles are closer than r_{\min} (RMIN), and
- their time-step becomes less than Δt_{\min} (DTMIN).

Both r_{\min} and Δt_{\min} are user-controlled parameters in N -body units (See Appendix D). We consistently choose $r_{\min} = 10^{-4}r_N$ and $\Delta t_{\min} = 10^{-5}t_N$ across all simulations presented here, suppressing an auto-adjustment during the run. Here, $r_N \approx 1.3R_{\text{hm}}$ and $t_N \approx 15 \text{ Myr} (r_N/M_{\text{Tot}})^{1/2}$ are N -body length and time unit, respectively, where R_{hm} is the half-mass radius of the star cluster, and M_{Tot} is the initial total mass in our simulations.

Our GW merger and TD models operate by examining the orbital properties of all objects within 10^{-4} pc when the

IMBH is in a “single” (i.e., not undergoing any close encounter that meet the criteria for KS regularization), or by analyzing the orbital properties of the companion object when the IMBH is in a KS regularized state. When the IMBH-BH binary undergoes a close encounter with other particles, their evolution is treated in the routine such as `triple`, `quad`, or `chain`. In this case, however, we do not apply our model, as such events are rare. See Appendix B for more justification.

If the IMBH is in a “single” state, we compute the semi-major axis a and eccentricity e of particles within a distance of 10^{-4} pc at every time-step in `intgrt.f`. If the IMBH forms a KS pair, we check the values of a and e for the binary during every call of the routine `ksint.f`. We then decide whether to merge the particles based on the corresponding criteria regardless of KS regularization. For a SBH, we calculate the merger timescale using the equation from Peters (1964) as

$$t_{\text{GW}} = \frac{5}{256} \frac{c^5 a^4 (1 - e^2)^{3.5}}{G^3 M_{\text{IMBH}} M_{\text{BH}} (M_{\text{IMBH}} + M_{\text{BH}})}, \quad (1)$$

where M_{IMBH} and M_{BH} refer to the masses of the IMBH and the SBH, respectively. Then the binary merges instantly if $t_{\text{GW}} < 1.0 \text{ Myr}$ during the run.² This timescale is sufficiently short to assume that the influence of the third particle on the binary is negligible. Therefore, we can safely consider that the binary evolves only through GW radiation. After the merger, we increase the mass of the IMBH by M_{BH} .

Although our primary goal is to investigate IMBH-BH collisions, implementing TD is necessary to properly consider and remove stars that are very close to the IMBH. In the case of an IMBH-star encounter, we compute the pericenter of the orbit as $r_p = a(1 - e)$. Then, we remove the star from the simulation if r_p is less than the tidal radius, r_T . The tidal radius is computed by $r_T = r_* (M_{\text{IMBH}}/M_*)^{1/3}$, where the stellar radius computed by $r_* = R_\odot (M_*/M_\odot)^{1/3}$ for a star with mass M_* . In this case, the mass of the IMBH is increased by half of the removed star’s mass, $0.5 M_*$. The choice of accreting a half of the stellar mass is based on analytical estimates (e.g., Rees 1988; Strubbe & Quataert 2009). The position and velocity of the IMBH are adjusted after a merger or a TD event in such a way that momentum conservation is guaranteed.

2.2. Signal-to-noise Ratios of Intermediate Mass Ratio Inspirals (IMRIs) at GW Observatories

The binary of BHs with masses M_1 and M_2 shrinks and circularizes by emitting energy as gravitational waves. If external perturbations are negligible, we can analytically predict their evolution based on the 2.5PN (2.5 post-Newtonian) ap-

¹ KS regularization is a treatment introduced to reduce the computational load during close encounters between particles. This should be distinguished from the merger criteria of the binaries described in the following paragraphs.

² See Appendix A for more justification

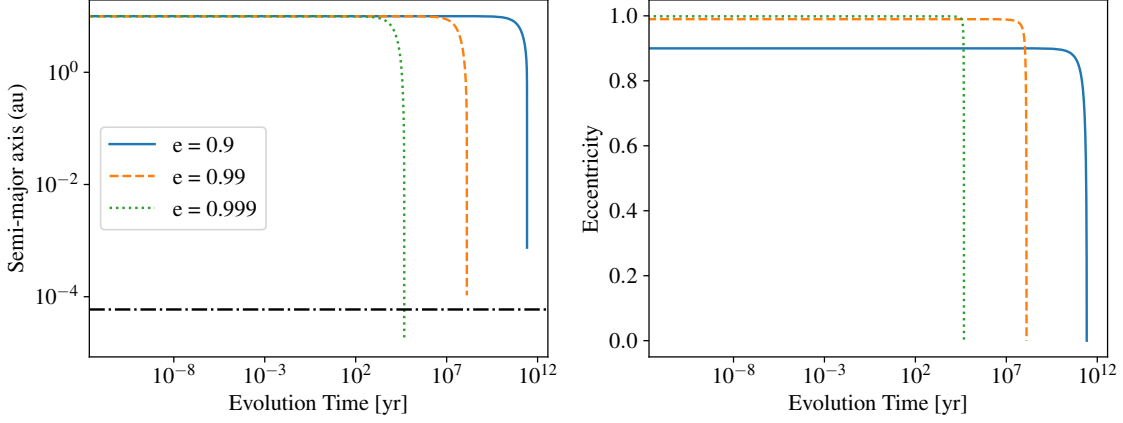


Figure 1. Comparison of the IMBH-BH binary evolution for different initial eccentricities based on Eqs.(F10) and (F11). All binaries have $M_{\text{IMBH}} = 10^3 M_{\odot}$ and $M_{\text{BH}} = 40 M_{\odot}$, and begin with $a = 10 \text{ au}$. *Left:* The closer the initial eccentricity of the binary is to 1, the shorter its merger timescale becomes (see Section 2.2). The *black dash-dotted line* refers to the Schwarzschild radius of the IMBH. The merger timescales estimated by Eq.(1) are $t_{\text{GW}} = 2.31 \times 10^{11} \text{ yr}$, $8.58 \times 10^6 \text{ yr}$, and $2.76 \times 10^4 \text{ yr}$, for $e = 0.9$, 0.99 , and 0.999 , respectively. *Right:* The evolution of eccentricity as the binary evolves in time. This figure shows the significant impacts of the initial eccentricity significantly on the merger timescale.

proximation. We compute the evolution of the IMRIs based on the orbit-averaged prescription provided by Peters (1964). Figure 1 depicts the evolution of the IMBH-BH binary with $a = 10 \text{ au}$ with three different eccentricities, as calculated from Eqs. (F10) and (F11). An IMRI with relatively modest eccentricity, $e = 0.9$, requires $\sim 10^{12}$ years to merge via pure GW radiation. In contrast, it takes less than 10^5 yr for a highly eccentric IMRI until the merger. The merger timescale of the binary is dramatically shorter for a more eccentric binary.

We then compute the sky-averaged signal-to-noise ratio (SNR) produced by the GW source at a luminosity distance D_L by combining the results from Finn & Thorne (2000) and Barack & Cutler (2004) as

$$\left(\frac{S}{N}\right)^2 = \sum_n \int h_{c,n}^2(f_n) \frac{d \ln f_n}{f_n}, \quad (2)$$

where $f_n = n f = n \sqrt{G(M_1 + M_2)/a^3}$ is the frequencies of the n -th harmonic, $h_{c,n} = (\pi D_L)^{-1} \sqrt{2 \dot{E}_n / f_n}$ is the characteristic amplitude of the n -th harmonic at distance D_L , \dot{E}_n is the energy radiated through the n -th harmonic, and $S_h(f)$ represents the noise spectral density of the detectors at frequency f .³ We explore the signals onto five detectors; aLIGO, ET, LISA, aSOGRO, and DECIGO. See Appendix H for more information. The integration domain of f starts 4 years before the binary reaches the innermost stable circular orbit (ISCO).

Figure 2 shows the evolution of the first five characteristic amplitudes, $h_{c,n}$ of an IMRI. The IMRI considered con-

sists of an IMBH with $M_{\text{IMBH}} = 10^3 M_{\odot}$ and a BH with $M_{\text{BH}} = 40 M_{\odot}$. The figure includes the curve of integrated GW signals and the intrinsic sensitivity curve for GW observatories. The GW frequency increases as the binary shrinks, and it remains in the LISA band for a period of time. The inspiral-plunge transition occurs approximately when the binary's orbital frequency crosses the ISCO frequency. The frequency of its 2nd harmonic is given by

$$f_{2,\text{ISCO}} = \frac{1}{\pi(1+z)} \sqrt{\frac{GM_{\text{IMBH}}}{R_{\text{ISCO}}^3}} \approx \frac{8.6}{1+z} \text{ Hz} \left(\frac{M_{\text{IMBH}}}{10^3 M_{\odot}}\right)^{-1}. \quad (3)$$

where $1/(1+z)$ reflects the effect of the redshift due to the expansion of the universe.

2.3. Modelling IMRI Detection Rates

Due to the limited computational resources, our star clusters should have smaller particle numbers and sizes than the realistic star clusters. Therefore, we try to mimic the GCs by analyzing the IMRI rates as a function of velocity dispersion given by the following form:

$$\Gamma_{\text{IMRI}} \propto M_{\text{IMBH}}^A \sigma_{\text{hm}}^B, \quad (4)$$

to establish an empirical relation estimating the IMRI rates (see Eq.(13) and Section 4.2). Here, σ_{hm} is the 1D half-mass velocity dispersion of the cluster.

Our simulations also provide statistics on the orbital properties of IMRIs, such as the eccentricities or the masses of secondary BHs. We then estimate the detection rate of these

³ The prefactor 5 emerges as a result of averaging the noise over all-source directions (Finn & Thorne 2000).

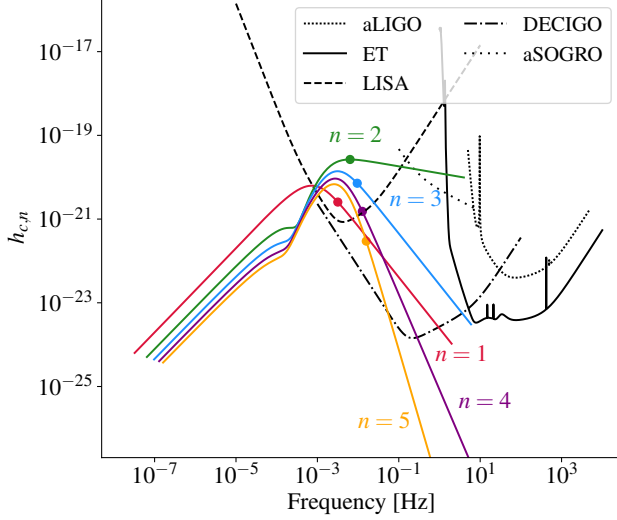


Figure 2. A sample illustration of the characteristic amplitude of the n -th harmonics, $h_{c,n}$, from $n = 1$ to 5 emitted during the IMRI. The dashed black V-shaped curve represents LISA’s sensitivity curve ($\sqrt{f}S_h(f)$; see Section 2.2), while two U-shaped curves indicate the sensitivities of aLIGO (densely-dotted line) and ET (solid line). Lastly, the intermediate frequency band from 10^{-3} Hz to 10^1 Hz is covered by two detectors; aSOGRO (loosely-dotted line) and DECIGO (dash-dotted line). The dots on the curve mark the moment 4 years before the merger. Here, we assume the IMBH mass to be $M_{\text{IMBH}} = 10^3 M_\odot$ and the secondary BH mass to be $M_{\text{BH}} = 40 M_\odot$. The binary system is initialized with a semi-major axis $a = 10$ au and an eccentricity $e = 0.999$, which is consistent with the green curve in Figure 1. The source is assumed to be located at a distance of 500 Mpc from us. This figure demonstrates that the IMRI stays in the LISA and DECIGO detection band for most of its evolution. While the aSOGRO and the ET can capture the last stable merger, aLIGO is mostly insensitive to this GW event.

events using the formula:

$$\begin{aligned} & \frac{d\Gamma_{\text{det}}}{dM_{\text{GC}} dM_{\text{IMBH}} dz} \\ &= p_{\text{IMBH}} f_{\text{det}}(M_{\text{IMBH}}, z) \Gamma_{\text{IMRI}}(M_{\text{IMBH}}, \sigma_{\text{hm}}) \\ & \times n_{\text{GC}} \frac{dv_{\text{GC}}}{dM_{\text{GC}}} \frac{dM_{\text{GC}}}{dM_{\text{IMBH}}} \frac{dV_c}{dz} \frac{1}{(1+z)}, \end{aligned} \quad (5)$$

which contains the following components:

- p_{IMBH} is the IMBH retention probability of GCs. The magnitude of the natal kick can be modeled as a Maxwellian distribution (Hobbs et al. 2005), or it can be derived from the mass fallback caused by the supernova explosion during the IMBH synthesis (Belczynski et al. 2002). About $\lesssim 30\%$ of GCs are expected to host IMBHs, and this probability may fall close to 0% for GCs with masses below $10^5 M_\odot$ (Giersz et al. 2015; Askar et al. 2017, 2022). We utilize the retention probability of IMBH formation depending on the star

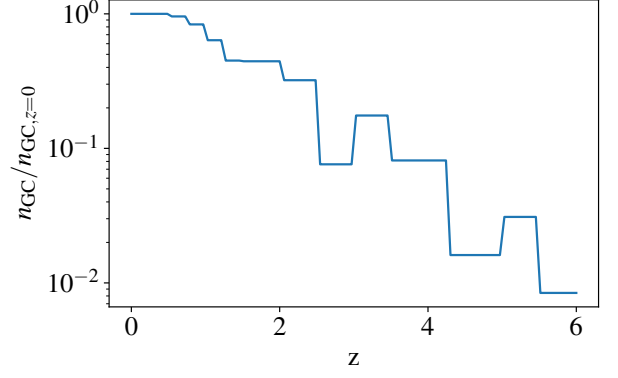


Figure 3. The evolution of the “normalized” GC number density, $v_{\text{GC}} \equiv n_{\text{GC}}/n_{\text{GC},z=0}$, from $z = 0$ to $z = 6$. The local GC number density $n_{\text{GC},z=0}$ is estimated based on the quantities such as the galaxy populations and the average fraction of galactic masses contained in GCs. The rebounds at $z = 3$, and $z = 4.5$ arise from the discords between different measurements; we choose (Tomczak et al. 2014) for $z = 0 - 3$, (Caputi et al. 2011) for $z = 3 - 4.5$, and (Song et al. 2016) for $z = 4.5 - 6$. See Section 2.3 for more information.

cluster mass considering both high and low natal kicks referring Table 1 in Askar et al. (2022).

- f_{det} is the fraction of IMRIs observable by a GW detector, which depends on M_{IMBH} , redshift z , and the specific detector design. We assume that detectable IMRIs must have a signal-to-noise ratio $S/N > 8$. This factor is modeled based on the distribution of orbital properties of IMRI events derived from our simulations.
- dv_c/dz is the comoving volume element at a given redshift bin, and $1/(1+z)$ accounts for the time dilation.
- n_{GC} is the number density of GCs in each redshift bin. Figure 3 presents the “normalized” GC number density, $v_{\text{GC}} \equiv n_{\text{GC}}/n_{\text{GC},z=0}$, at each redshift bin, while the absolute value of n_{GC} depends on the estimation of local GC density. Indeed, the GC number density at $z = 0$ varies across studies — from 0.77 Mpc^{-3} (Rodríguez et al. 2015) to $8.4 h^3 \text{ Mpc}^{-3}$ (Portegies Zwart & McMillan 1999). In our approximation, assuming GCs with masses 5×10^4 to $8 \times 10^6 M_\odot$ account for 0.1% of the galaxy mass, we obtain $n_{\text{GC},z=0} = 1.45 \text{ Mpc}^{-3}$. Note that the average mass of these GCs becomes $\langle M_{\text{GC}} \rangle = 1.9 \times 10^5 M_\odot$ here. We also model the halo mass function, $\phi(\bar{M}, z)$, by the Schechter (1976) function (see Appendix E for detailed information), with the parameters adopted from Table.(1) of Conselice et al. (2016). More details about n_{GC} can be found in Appendix G.
- $dv_{\text{GC}}/dM_{\text{GC}}$ refers to the normalized GC mass function. We assume that it follows a simple power-law,

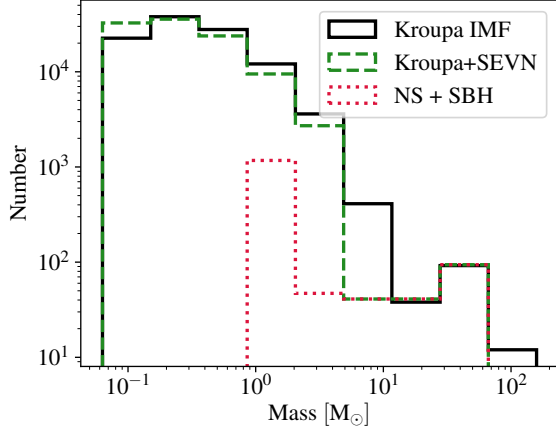


Figure 4. The distribution of stellar populations sampled from the Kroupa IMF (*solid-black*) with mass ranges $0.08 - 150 M_{\odot}$. The population after evolving 100 Myr loses some of its heavy components and the maximal mass decreases to $60 M_{\odot}$ due to the mass loss during evolution (*dashed-green*). Especially, compact objects (*dotted-red*) such as stellar-mass black holes (SBHs) or neutron stars (NSs) that are subject to GW merger are evenly distributed over the mass ranges $0.8 - 60 M_{\odot}$.

$dV_{GC}/dM_{GC} \propto M_{GC}^{-s}$ with a slope parameter $s = 2.2$ (Gieles 2009).

- dM_{GC}/dM_{IMBH} models the relation between M_{IMBH} and M_{GC} . To simplify our calculation, here we use the linear relation from Arca-Sedda (2016),

$$\log\left(\frac{M_{IMBH}}{M_{\odot}}\right) = \log\left(\frac{M_{GC}}{M_{\odot}}\right) - 2.23. \quad (6)$$

According to this relation, IMBHs of $300 - 5000 M_{\odot}$ correspond to the GCs of masses $5 \times 10^4 - 10^6 M_{\odot}$.

3. INITIAL CONDITIONS

3.1. Star Cluster Parameters and Computational Optimizations

We generate the initial conditions of the star cluster using the code MCLUSTER (Küpper et al. 2011). The simulated star clusters are designed to follow the Plummer profile,

$$\rho_P(r) = \frac{3M_{SC}}{4\pi a_P^3} \left(1 + \frac{r^2}{a_P^2}\right)^{-2.5}, \quad (7)$$

where M_{SC} and a_P refer to the total mass and scale size of the star cluster, respectively. The half-mass radius R_{hm} of the Plummer cluster is approximated by $1.3a_P$. We initialize the clusters without including primordial mass segregation or binaries.

To construct a realistic SBH mass function, we generate the stellar population by sampling from the Kroupa (2001)

Table 1. Initial conditions of our simulation suite. Both Groups A and B investigate the influence of the star cluster properties and the IMBH mass on the GW merger rate, respectively. Each simulation has been tested over 10 random seeds. The initial half-mass velocity dispersion is calculated for particles within R_{hm} from the IMBH after the “adiabatic” insertion. Although the star clusters are initially generated by identical properties (Group B), the velocity dispersion is affected by the mass of IMBHs.

Name [†]	M_{GC} (M_{\odot})	N_{star} (10^4)	R_{hm} (pc)	σ_{hm} (km s^{-1})	$M_{IMBH,i}$ (M_{\odot})	t_{term} (Myr)
A-i	5×10^4	10.5	0.5	8.52	1000	30
A-ii ^a	5×10^4	10.5	0.7	7.27	1000	30
A-iii	5×10^4	10.5	1.0	6.07	1000	30
A-iv	10^5	21.0	0.7	10.06	1000	30
A-v	10^5	21.0	1.0	8.41	1000	30
B-i	5×10^4	10.5	0.7	7.06	300	30
B-ii	5×10^4	10.5	0.7	7.15	500	30
B-iii	5×10^4	10.5	0.7	7.27	1000	30
B-iv	5×10^4	10.5	0.7	7.56	2000	30
B-v	5×10^4	10.5	0.7	7.84	3000	30
B-vi	5×10^4	10.5	0.7	8.30	5000	30

NOTE— [†]The list of simulations performed for this study. Col. 1: Names of simulations. Col. 2-3: Total mass and total number of particles in the star cluster. Col. 4-5: Half-mass radius and initial 1D half-mass velocity dispersion of the cluster. Col. 6: Initial mass of an embedded IMBH. Col. 7: Termination time of the simulation.

^a Identical to B-iii

initial mass function (IMF) within stellar mass range of $0.08 - 150 M_{\odot}$. We then evolve the stars using the stellar evolution code SEVN (Spera et al. 2019; Iorio et al. 2023) over 100 Myr. Figure 4 presents the mass function before and after stellar evolution. It reveals that the neutron stars (NSs) and SBHs are spread over the mass range from $0.8 M_{\odot}$ to $60 M_{\odot}$. Most stars with initial masses above $10 M_{\odot}$ turn into the BHs, with their final mass decreasing by the effect of the pair-instability supernova (PISN) or pulsational pair-instability supernove (PPISN) (e.g., Woosley 2017; Woosley & Heger 2021). Meanwhile, the NSs dominate the lower-mass end of the compact object spectrum. Since our simulations run over a relatively short timescale up to 30 Myr, we suppress further stellar evolution during our experiments. This is because stellar evolution processes extend over significantly longer timescales and are beyond the primary focus of our study.

The typical mass range of GCs is a few $\times 10^3$ to $5 \times 10^6 M_{\odot}$ with a scale radius of ~ 3 pc. However, higher-mass GCs still need $\gtrsim \ell$ (10^5) particles to be simulated. We therefore mimic the dense environment of GCs by reducing the size of GCs instead of increasing their mass. This approach allows us to maintain a manageable number of particles resolved in

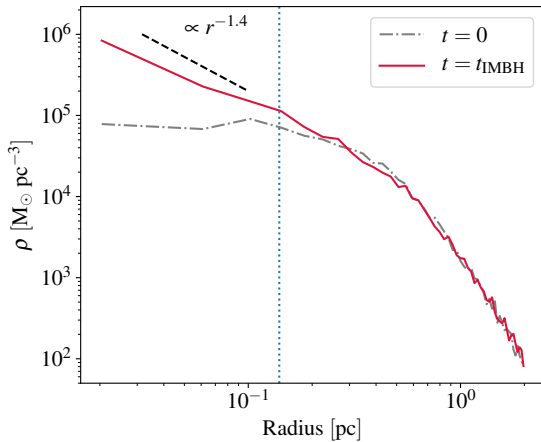


Figure 5. The radial density profile of the GC before (*grey dash-dotted*) and after (*red*) the “adiabatic growth” of a star cluster to introduce an IMBH (see Section 3.2 for more information). The star cluster has a mass of $5 \times 10^4 M_\odot$ and a half-mass radius of 0.7 pc. The IMBH mass when it is introduced as a live particle is $M_{\text{IMBH},i} = 10^3 M_\odot$. The inner profile of the star cluster is flat at $t = 0$, whereas it is deformed to follow a power-law profile at $t = t_{\text{IMBH}}$ ($= 50 t_N$; see Section 3.2). The simulated star cluster has a slope of $\gamma \approx 1.4$, less steep than the theoretically expected value of $\gamma = 1.75$. The *vertical dotted line* refers to the IMBH’s radius of gravitational influence.

simulations, thus reducing computational costs. We note that the overall evolution of the star cluster is significantly influenced by its total mass. However, the effect of the different GC masses on the GC evolution can be marginalized, as we terminate our simulations after only $t_{\text{term}} = 30$ Myr (more discussion in Section 4.1).

We explore the IMRI rates in various stellar system settings, by changing its initial half-mass velocity dispersion from $\sigma_{\text{hm}} \sim 6 \text{ km s}^{-1}$ to $\sim 10 \text{ km s}^{-1}$ (Group A in Table 1), and by varying the initial IMBH mass from $M_{\text{IMBH},i} = 300 M_\odot$ to $5000 M_\odot$ (Group B in Table 1). Before inserting the IMBH, we gradually modify the GC centers by slowly increasing the point mass potential, in order to avoid the sudden introduction of a massive object (as described in Section 3.2). All our simulated star clusters are initialized in isolation, with no external tidal fields included.

3.2. Adiabatic Growth of A Star Cluster To Introduce An Embedded IMBH

Both observational (e.g., Schödel et al. 2009) and theoretical (e.g., Bahcall & Wolf 1976) studies agree that star clusters with a massive central object exhibit steeply increasing profiles for density and velocity dispersion toward the center. Sigurdsson et al. (1995) suggested that an “adiabatically growing” density profile can be a reasonable way to realize an N -body system with an IMBH. First, before inserting the

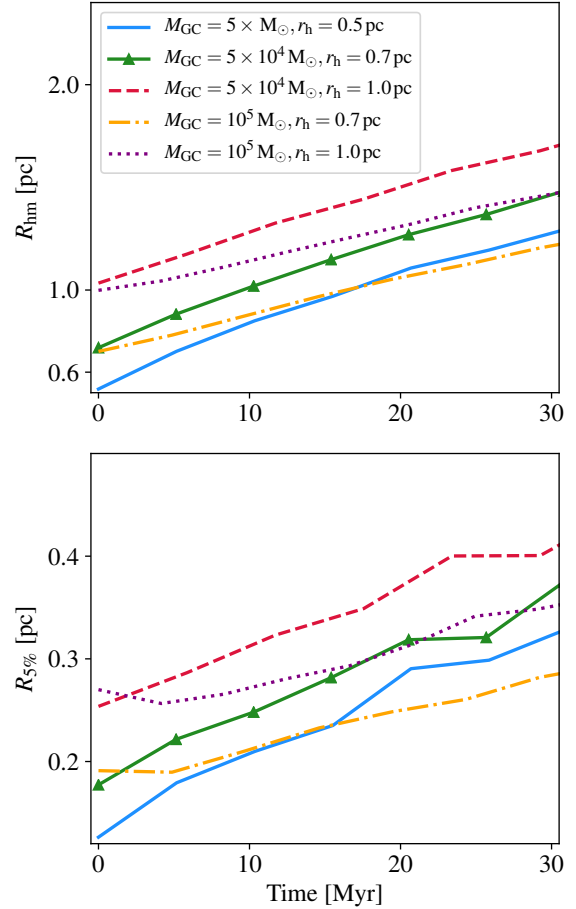


Figure 6. This plot depicts the evolution half-mass radii (*top*) and the radius enclosing 5% of the initial cluster mass (*bottom*) for Group A. Each curve is averaged over all 10 random seeds, and the mass of the IMBH is excluded from the calculations. The overall increase of the radius shows the expansion of the stellar systems.

IMBH as a live particle, we generate the initial condition of star clusters following a Plummer density profile using MCLUSTER. Then we introduce the Plummer potential with a gradually increasing mass $M_{\text{IMBH}}(t)$ as

$$\phi_{\text{IMBH}} = -\frac{GM_{\text{IMBH}}(t)}{(r^2 + \epsilon_{\text{IMBH}}^2)^{1/2}}, \quad (8)$$

where $\epsilon_{\text{IMBH}} \sim 10^{-4}$ pc is the softening parameter placed to avoid the effect of the singularity (Hong & Lee 2015). Then, t_{IMBH} after the initialization, we replace the external potential with a live, moving IMBH particle. Here, the time-dependent IMBH mass is designed to grow over time as

$$M_{\text{IMBH}}(t) = M_{\text{IMBH},i} \left[3 \left(\frac{t}{t_{\text{IMBH}}} \right)^2 - 2 \left(\frac{t}{t_{\text{IMBH}}} \right)^3 \right], \quad (9)$$

where $M_{\text{IMBH},i}$ is the initial mass of the IMBH when it is finally inserted as a live particle, and t_{IMBH} is the mass growth

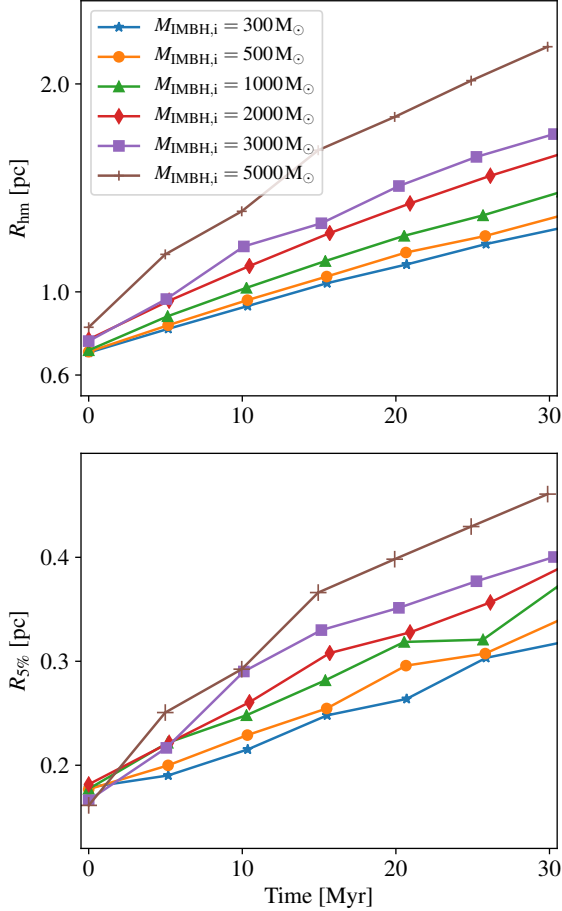


Figure 7. The same set of plots as presented in Figure 6, but now corresponding to Group B.

timescale. Any choice of t_{IMBH} is suitable as long as it is not too short (Sigurdsson et al. 1995), thus we set it to be $t_{\text{IMBH}} = 50t_N$. This is a relatively short timescale in our simulations, \sim a few Myrs. The definition of the N -body units can be found in Appendix D. Figure 5 shows an example of “adiabatic growth” of a star cluster to introduce an embedded IMBH. At $t = 0$, the cluster core has a flat density profile. As the analytic IMBH potential gradually grows, the inner profile evolves into a cuspy profile of $\rho \propto r^{-\gamma}$ with a slope index $\gamma \approx 1.4$. This is slightly shallower than the classical prediction by Bahcall & Wolf (1976), $\gamma = 1.75$. This difference can be attributed to the nature of the star clusters consisting of stars with different masses (Baumgardt et al. 2004a).

4. RESULTS

Now we present the results of our simulations and discuss the possibility of detecting IMRIs through each of the existing and future GW telescopes.

4.1. Evolution of A Star Cluster System

We begin by examining the temporal evolution of the star clusters. The characteristic timescale for the evolution can be estimated by the relaxation timescale, t_{rlx} , which is defined as

$$t_{\text{rlx}} = \frac{\sqrt{2}\sigma^3(r)}{\pi G^2 \langle M_* \rangle \rho(r) \ln \lambda} \quad (10)$$

where $\sigma(r)$ is the local velocity dispersion, $\langle M_* \rangle$ is the average stellar mass, $\rho(r)$ is the mass density, and $\ln \lambda \approx 10$ is the Coulomb logarithm. This expression suggests that denser star clusters evolve more rapidly compared to less dense clusters.

The evolution of the half-mass radius, R_{hm} , and the Lagrangian radius enclosing 5% of the initial cluster mass, $R_{5\%}$ of runs in Group B is depicted in Figure 6. These radii serve as key indicators of the structural evolution of star clusters over time. In general, the star clusters undergo expansion due to the relaxation processes. The rate of this expansion notably depends on the cluster’s relaxation timescale. For example, the GCs with initial properties $M_{\text{GC}} = 5 \times 10^4 M_\odot$ and $R_{\text{hm}} = 0.7 \text{ pc}$ undergoes an expansion of R_{hm} from 0.7 pc to 1.3 pc. In contrast, the GCs with initial properties $M_{\text{GC}} = 10^5 M_\odot$ and $R_{\text{hm}} = 0.7 \text{ pc}$ expands from $R_{\text{hm}} = 0.7 \text{ pc}$ to only $R_{\text{hm}} = 1.0$, reflecting the relaxation timescale determined by the GC mass.

The evolution of the simulations in Group B is illustrated in Figure 7. All simulations are initialized with the same $R_{5\%}$ and R_{hm} at $t = 0$ except for the small discrepancies caused by the adiabatic insertion of IMBH before initialization (See 3.2). As the GC evolves, the rate of expansion of the cluster size varies across different $M_{\text{IMBH},i}$. For a lower-mass IMBH ($M_{\text{IMBH},i} = 300 M_\odot$), the half-mass radius increases from $R_{\text{hm}} = 0.7 \text{ pc}$ to $R_{\text{hm}} = 1.1 \text{ pc}$. For a more massive IMBH ($M_{\text{IMBH},i} = 5000 M_\odot$), the half-mass radius grows significantly more, reaching $R_{\text{hm}} = 2.1 \text{ pc}$. This trend highlights the crucial role of IMBH mass in driving the dynamical expansion of the host GC as discussed in previous studies (e.g., Baumgardt et al. 2004b; Freitag et al. 2006a; Hong & Lee 2015).

The detailed evolution of the cluster core is depicted in Figure 8. The two left panels display the evolution of the central density, ρ_c , for the populations within $r < R_{5\%}$ from the cluster’s center. In all simulations, the central density decreases monotonically as the core expands over time. The evolution of the central density is significantly affected by both the initial star cluster properties and the mass of the central IMBHs. This trend is already expected from the evolution of $R_{5\%}$ (See Figure 6 & 7).

The right panel of Figure 8 presents the evolution of the central velocity dispersion, σ_c . Unlike the central density, the overall evolution of σ_c exhibits a more gradual and steady decline over time. In Group A, the evolution of σ_c closely follows the trend of central density decline, supporting the

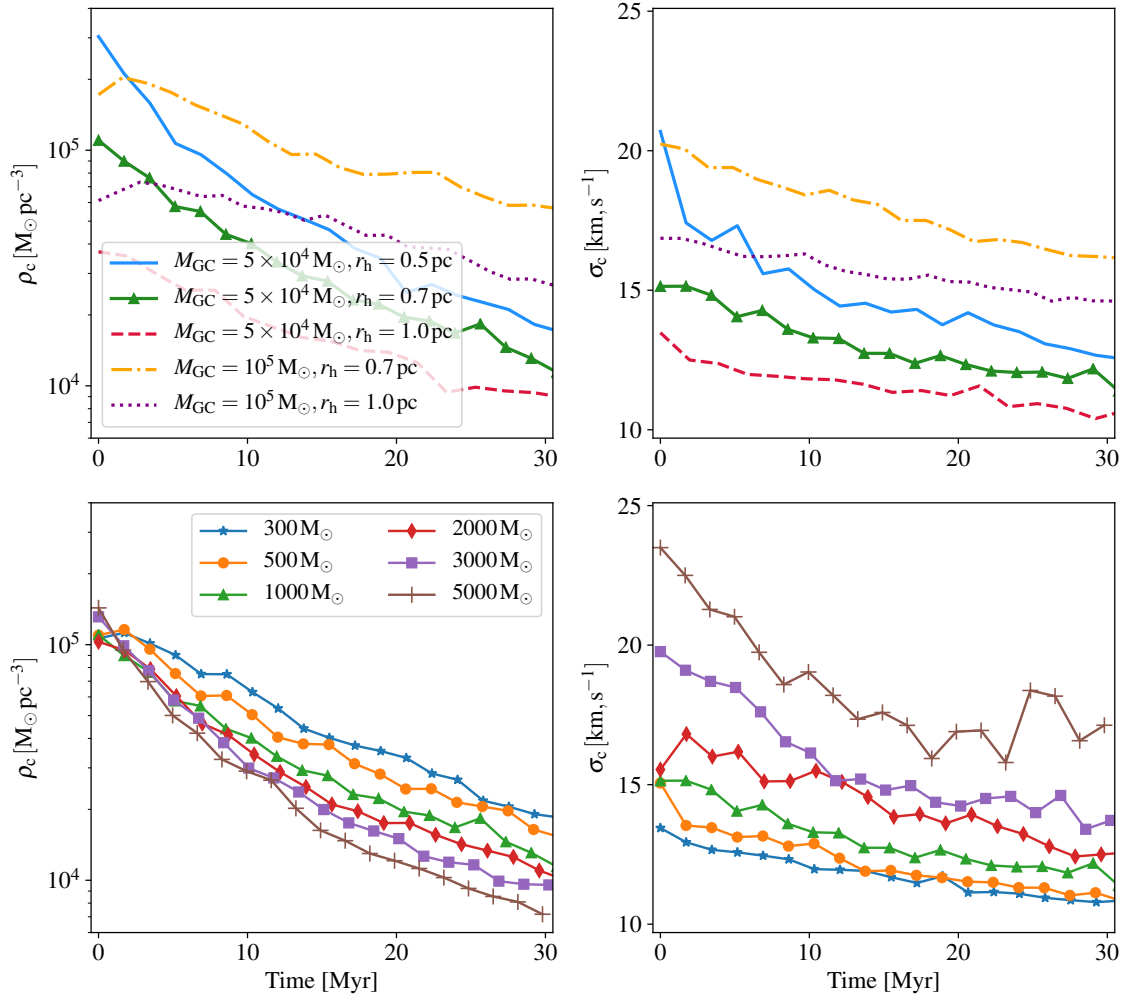


Figure 8. The evolution of the mean density (*left*), and the (1D) velocity dispersion (*right*) near the cluster center for both group A (*top*) and Group B (*bottom*). These quantities are computed over the population except for the IMBH within $r < R_{5\%}$ from the center. In general, the cluster density and velocity dispersion decrease over time due to the expansion of the star clusters. Both the density and velocity dispersion within $r < R_{5\%}$ are significantly affected by the initial cluster properties while it is less affected by the initial mass of the IMBH. In Group A, the variations in density and velocity dispersion across different runs suggest that the initial parameters of the star clusters play a dominant role in determining the long-term evolution of the cluster core. In Group B, the more rapid decrease of density for higher-mass IMBH demonstrates the faster expansion of the star clusters. For an IMBH mass of $M_{\text{IMBH},i} = 5000 M_\odot$, the initial velocity dispersion of the stars near the cluster center reaches $\sim 24 \text{ km s}^{-1}$. In contrast, for lower-mass IMBHs, such as $M_{\text{IMBH},i} = 300 M_\odot$, the initial velocity dispersion is significantly lower, reaching only $\sim 14 \text{ km s}^{-1}$. See Section 4.1 for more information.

interpretation that the decrease in velocity dispersion is primarily driven by the expansion of the cluster core. As in the central density, the velocity dispersion of the clusters with longer t_{rlx} experiences more gradual dynamical evolution. For example, the GC with a total mass $M_{\text{GC}} = 5 \times 10^4 M_\odot$ and an initial half-mass radius of $R_{\text{hm}} = 0.5 \text{ pc}$ undergoes a more than 30% reduction in central velocity dispersion, decreasing from 20 km s^{-1} to 13 km s^{-1} . In contrast, the GCs with the same mass but a larger initial half-mass radius of $R_{\text{hm}} = 1 \text{ pc}$ experiences a relatively smaller ($\sim 20\%$) decline, with σ_c decreasing from 14 km s^{-1} to 11 km s^{-1} .

In Group B, the presence of an IMBH introduces additional dynamical effects. The strong gravitational potential of a massive IMBH significantly enhances the velocity dispersion of stars near it, leading to distinct differences in the initial values of σ_c depending on the IMBH mass. For an IMBH with $M_{\text{IMBH}} = 5000 M_\odot$, the initial central velocity dispersion is $\sim 24 \text{ km s}^{-1}$ at $t = 0 \text{ Myr}$, gradually decreasing to 18 km s^{-1} by $t = 30 \text{ Myr}$ as cluster expands. In contrast, for an IMBH with $M_{\text{IMBH},i} = 300 M_\odot$, the initial velocity dispersion is significantly lower, starting at $\sim 14 \text{ km s}^{-1}$ at $t = 0 \text{ Myr}$ and declining more modestly to 11 km s^{-1} by $t = 30 \text{ Myr}$. In summary, our result suggests that the evolu-

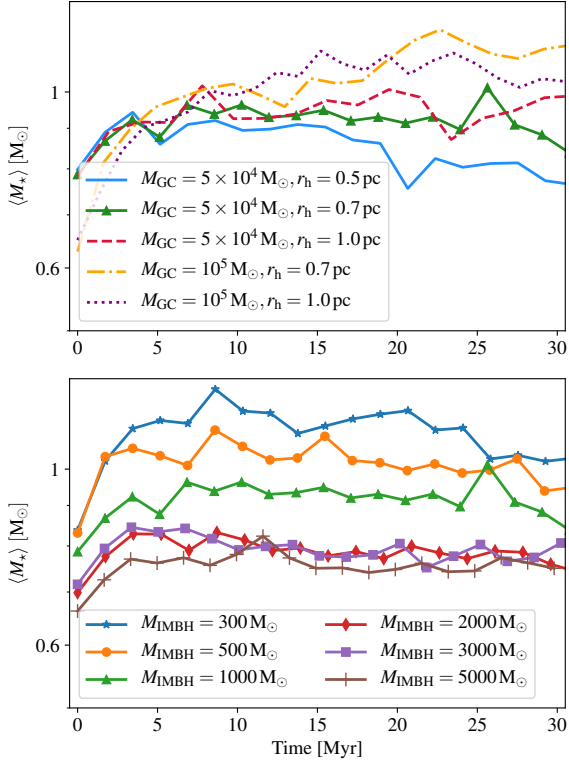


Figure 9. The figure illustrates the evolution of the mean mass, $\langle M_{\star} \rangle$, of stars and SBHs within a radius of $r < R_{5\%}$ presented separately for Group A (*top*) and Group B (*bottom*). In general, $\langle M_{\star} \rangle$ exhibits a rapid increase in the early stage of evolution, stabilizing by $t = 10$ Myr across all simulations. In the top panel, $\langle M_{\star} \rangle$ gradually diverges over time, reflecting the influence of the initial properties of the GCs on their long-term evolution. Conversely, the bottom panel shows a decreasing trend in $\langle M_{\star} \rangle$ with increasing M_{IMBH} , suggesting that the presence of a more massive IMBH influences the retention and distribution of stellar populations within the core region. The initial discrepancy at $t = 0$ is attributed to the evolution of star clusters during the adiabatic growth of IMBH.

tion of the cluster center is highly governed by the properties of GCs, and the mass of the IMBH exerts a significant gravitational influence on the stars in its vicinity.

Figure 9 displays the evolution of the average mass of stars and SBHs within $R_{5\%}$ from the center. The mean stellar mass exhibits a rapid increase early on and stabilizes by 10 Myr in all simulations. In the top panel, the initial mean stellar mass differs between clusters of different total masses, being higher in the $5 \times 10^4 M_{\odot}$ GCs compared to the $10^5 M_{\odot}$ cluster. This discrepancy reflects a more rapid relaxation process during the adiabatic growth of IMBH prior to the initialization of simulations (See Section 3.2). Across all simulations in Group A, the central mean stellar mass stabilizes commonly at $\langle M_{\star} \rangle \sim 0.9 M_{\odot}$. However, the subsequent evolution of the mean stellar mass depends on the initial properties of the star cluster, reaching values between $\sim 0.7 M_{\odot}$ and $\sim 1 M_{\odot}$ by $t = 30$ Myr. Meanwhile, the lower panel high-

lights a clear decreasing trend in the average stellar mass at the cluster center with increasing IMBH mass. This demonstrates a significant influence of IMBH mass on the mean stellar mass at the cluster center.

We now explore the implications of the initial conditions of a star cluster on the motion of an IMBH. One key parameter is the IMBH’s distance from the center, or the wandering radius, representing the typical distance the IMBH moves from the cluster center due to gravitational interactions with surrounding stars. The wandering radius of the IMBH can be estimated using the following equation (Stone et al. 2017):

$$d_{\text{IMBH}} \approx R_c \left(\frac{\langle M_{\star} \rangle}{M_{\text{IMBH}}} \right)^{1/2}. \quad (11)$$

While the equation originally uses R_c as the core size of the star cluster, there is ambiguity in how the core is defined for a star cluster in our simulations. Therefore, we instead adopt $R_{5\%}$ as a practical proxy. The top-left panel of Figure 10 confirms that the wandering radius increases with the size of the star clusters, consistent with our expectation that larger cores provide more room for the IMBH to move around. The bottom-left panel, however, does not show a clear dependence of d_{IMBH} on M_{IMBH} , even though Equation 11 predicts an inverse-square-root scaling.

The principle of energy equipartition provides an estimate for the speed of the IMBH, $|v_{\text{IMBH}}|$ as follows:

$$|v_{\text{IMBH}}| = \sigma_{c,3D} \left(\frac{\langle M_{\star} \rangle}{M_{\text{IMBH}}} \right)^{1/2} \quad (12)$$

where $\langle M_{\star} \rangle$ is the average stellar mass, and $\sigma_{c,3D}$ is the 3D velocity dispersion of the stellar system given by $\sigma_{c,3D} = \sqrt{3}\sigma_c$. The two left panels in Figure 10 illustrate the evolution of the velocity dispersion in Group A and Group B, respectively. In Group A, $|v_{\text{IMBH}}|$ exhibits a mild decreasing trend with increasing GC size for fixed M_{GC} . Meanwhile, Group B shows a clear inverse dependence on M_{IMBH} , consistent as expected by Equation 12. However, the scales of IMBH’s wandering radius and the measured speeds in both groups are found to be an order of magnitude larger than the estimates provided by Equations 11 & 12. For example, inserting $M_{\text{IMBH},i} = 1000 M_{\odot}$, $\langle M_{\star} \rangle = 1.0 M_{\odot}$, and $\sigma_c = 14 \text{ km s}^{-1}$ (as seen for $M_{\text{IMBH},i} = 1000 M_{\odot}$ in Group B) into Equation 12, we obtain $|v_{\text{IMBH}}| \approx 1 \text{ km s}^{-1}$. This theoretical estimate is slightly lower than the measured value of $|v_{\text{IMBH}}| \approx 3 \text{ km s}^{-1}$ presented in the bottom right panel of Figure 10. This suggests that additional effects such as close encounters with SBHs might be influencing the IMBH’s motion beyond the simple equipartition model.

The evolution of the GC cores in the real universe might not be as rapid as seen in these simulations, because the real GCs have longer relaxation timescales due to their greater masses. The shortened relaxation time is an artifact of our

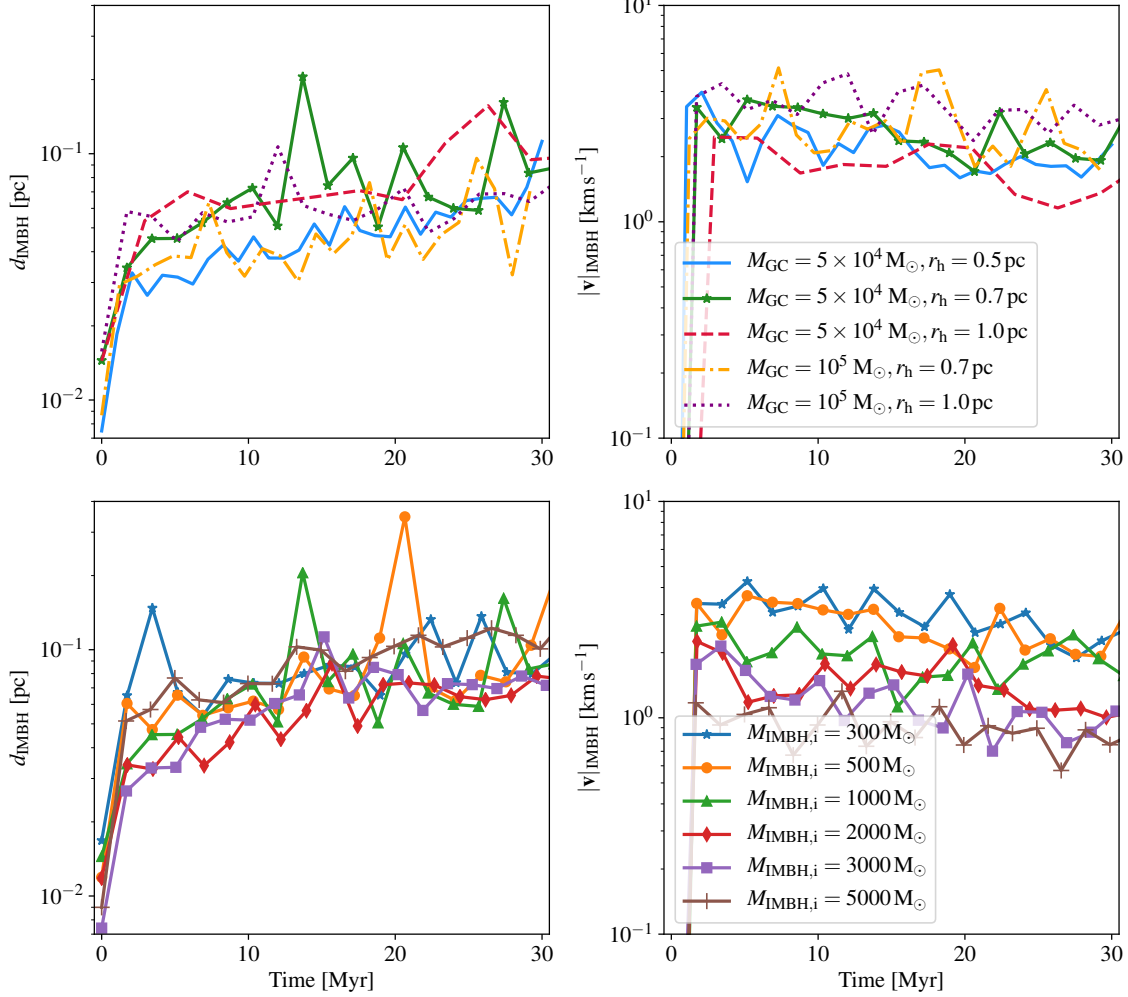


Figure 10. The evolution of the IMBH’s distance (*left*) from the center of mass of the star cluster and IMBH’s speed (*right*), considering Group A (*top*) and Group B (*bottom*). The IMBH is slightly off ($\lesssim 0.1$ pc) from the center of the GC both in Group A and Group B. The dynamics of IMBHs show a weak dependence on the cluster properties in Group A, while they show a clear dependence on M_{IMBH} in Group B. Although the overall trend is well predicted by Equation 12, its scale is approximately an order of magnitude greater than the estimation.

simulation design as discussed in Section 3.1. However, as we focus only on the central region surrounding the embedded IMBHs, and the statistical properties of IMRIs during the short runtime, we expect that our chosen GC properties would not significantly affect the conclusion from our analyses.

4.2. The Statistical Properties of IMRI Events

In this section, we explore the rates and statistical properties of the IMRIs derived from our suite of N -body simulations. Figure 11 depicts the IMRI event rates, Γ_{IMRI} , in the GCs with initial 1D half-mass velocity dispersions ranging $\sigma_{\text{hm}} \sim 6 \text{ km s}^{-1}$ to $\sim 10 \text{ km s}^{-1}$ (Group B in Table 1). They are calculated from the stellar and SBH populations within the half-mass radius in each simulation. Each data point represents a value averaged over 10 different random initializations. The initial mass of the IMBH is $M_{\text{IMBH},i} = 1000 M_{\odot}$.

Here we observe that Γ_{IMRI} increases with σ_{hm} . The IMRI rate is approximately $\sim 0.06 \text{ Myr}^{-1}$ in a cluster system with $\sigma_{\text{hm}} \sim 6 \text{ km s}^{-1}$, but it rises to $\sim 0.2 \text{ Myr}^{-1}$ in a cluster with $\sigma_{\text{hm}} \sim 10 \text{ km s}^{-1}$. This trend suggests that denser clusters, characterized by higher velocity dispersions, are more conducive to the IMRI formation.

Figure 12 highlights the relation between M_{IMBH} and Γ_{IMRI} for fixed cluster properties. The IMRI event rate increases from $\sim 0.08 \text{ Myr}^{-1}$ for a IMBH with $M_{\text{IMBH},i} = 300 M_{\odot}$ to $\sim 0.2 \text{ Myr}^{-1}$ for $M_{\text{IMBH},i} = 5000 M_{\odot}$. By integrating all our simulation results and fitting them to Eq.(4), we obtain the best linear fit that estimates the IMRI event rate:

$$\Gamma_{\text{IMRI}} = 0.06 \text{ Myr}^{-1} \left(\frac{\sigma_{\text{hm}}}{6 \text{ km s}^{-1}} \right)^{2.72} \left(\frac{M_{\text{IMBH},i}}{10^3 M_{\odot}} \right)^{0.15}. \quad (13)$$

Note that this relation is built by employing a limited IMBH mass range from $300 M_{\odot}$ to $5000 M_{\odot}$. Although it remains

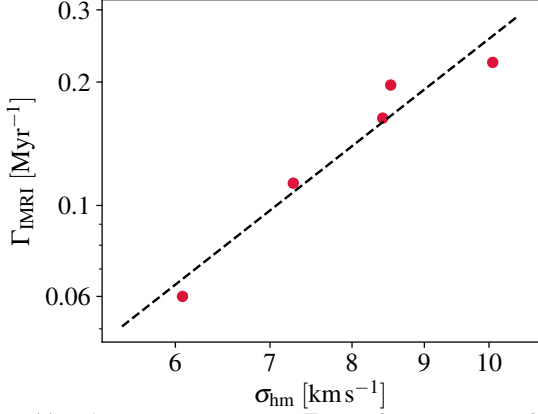


Figure 11. The IMRI event rates, Γ_{IMRI} , for an IMBH of initial mass $10^3 M_\odot$ embedded in the GCs with initial half-mass velocity dispersion $\sigma_{\text{hm}} \sim 6 \text{ km s}^{-1}$ to $\sim 10 \text{ km s}^{-1}$ (Group B in Table 1). Each data point is averaged over 10 random seeds. The *black dashed line* is the linear fit, indicating a clear positive correlation between σ_{hm} and Γ_{IMRI} . See Section 4.2 for more information.

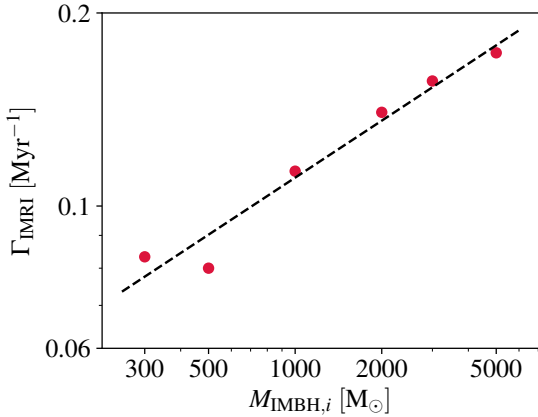


Figure 12. The IMRI event rates, Γ_{IMRI} , for an initial IMBH of mass 300 to $5000 M_\odot$ embedded in the GCs with a mass $5 \times 10^4 M_\odot$ and a half-mass radius 0.7 pc (Group C in Table 1). Each data point is averaged over 10 random seeds. The *black dashed line* is the linear fit, indicating a positive correlation between $M_{\text{IMBH},i}$ and Γ_{IMRI} . See Section 4.2 for more information.

uncertain whether this relation can be extrapolated to the IMBH masses beyond this range, our linear-fit is sufficient to predict the lower mass IMBHs that would occupy the majority of the IMBH population, which is more sensitive to the nature of natal kick. See Section 5.2 for more information.

We now study the orbital properties of the IMRI events from our suite of N -body simulations. The left panel of Figure 13 displays a histogram of the orbital eccentricities found in all of our simulations of Group B (see Table 1). It shows that the majority of the IMRIs have high eccentricities, $(1-e) \sim 10^{-3} - 10^{-4}$, at 1 Myr before the final merger. Binaries with even higher eccentricities, $(1-e) \lesssim 10^{-5}$, are less common because it is expected that such high values are

more difficult to achieve in the first place. Similarly, encounters with lower eccentricities, $(1-e) \gtrsim 10^{-2}$, are uncommon because they need to achieve an extremely tiny semi-major axis to satisfy our merger criteria (i.e., only the binaries with $t_{\text{GW}} < 1.0 \text{ Myr}$ are merged in the simulation; see Section 2.1). To validate this, in the middle panel of Figure 13 we show a relationship between the semi-major axes a and the eccentricities e from all Group B simulations. Requiring $t_{\text{GW}} = 1.0 \text{ Myr}$ for a fixed combination of M_{IMBH} and M_{BH} provide us with a relation $a^4 (1-e)^{3.5} = \text{constant}$ (see Eq.(1) in Section 2.1; here we assume $(1-e) \ll 1$). Indeed, the black dashed line marks such a relation for $M_{\text{IMBH}} = 10^3 M_\odot$ and $M_{\text{BH}} = 60 M_\odot$ with $t_{\text{GW}} = 1.0 \text{ Myr}$. As expected, we observe that most data points are located below this line. Lastly, the right panel of Figure 13 presents the mass distribution of the secondary BHs involved in the IMRI event. We find that an IMBH tends to form a binary with the most massive BHs in the star cluster.

5. DISCUSSION

Here we estimate the actual detection rate of the IMRI events by the ground- and space-based GW observatories.

5.1. Horizon Redshifts for IMRI Detection

Figure 14 presents the fraction of observable IMRI events for different GW telescopes, assuming events are detectable if its SNR is larger than 8 (Eq.(2) in Section 2.2). In the first panel, aLIGO is unable to detect IMBHs with $M_{\text{IMBH}} \gtrsim 500 M_\odot$ because its detection band is limited to frequencies $\gtrsim 10 \text{ Hz}$. Even for $M_{\text{IMBH}} \lesssim 300 M_\odot$, it can only detect very close IMRIs in the local universe ($z \lesssim 0.06$). Consequently, we can reasonably conclude that aLIGO would not be able to discover a merger event involving an IMBH, unless there is one with mass $\lesssim 300 M_\odot$ in the vicinity of Milky Way ($\lesssim 260 \text{ Mpc}$).

ET has a better capability to detect IMRIs compared to aLIGO, especially in the lower-mass range of M_{IMBH} . For example, the second panel of Figure 14 shows that it has the potential to detect almost all $300 M_\odot$ IMBHs up to $z \sim 1.0$, and some up to $z \sim 1.5$. ET also offers a relatively wider detection mass spectrum up to $M_{\text{IMBH}} \sim 2000 M_\odot$, although the horizon redshift decreases to $z \lesssim 0.1$. Note that the maximum redshift of detection — or the “horizon redshift” — decreases as M_{IMBH} increases.

On the other hand, we find that LISA, aSOGRO, and DECIGO can observe all IMRIs involving IMBHs across the entire mass range explored. However, their horizon redshifts vary significantly from each other. Figure 15 illustrates the horizon redshifts of each GW observatory across the IMBH masses $M_{\text{IMBH}} = 300 M_\odot$ to $10^4 M_\odot$. LISA has a growing horizon redshift for increasing M_{IMBH} from $z \sim 0.2$ to ~ 0.5 . Especially, it can better cover the detection of

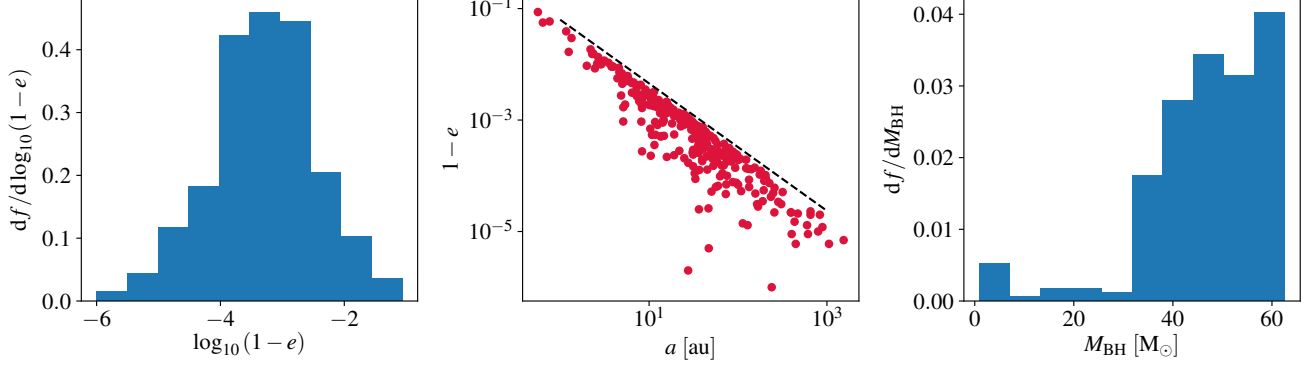


Figure 13. The distribution of the orbital parameters of all the IMRI events in all simulations of Group A (see Table 1). The *left panel* shows the distribution of eccentricities, peaking at $(1-e) \sim 10^{-3}$. The *middle panel* displays the scatter plot of the semi-major axes a versus eccentricities e , showing that a large number of eccentric binaries are formed by the IMBH. The *black dashed line* indicates a boundary on which the merger timescale t_{GW} (Eq.(1) in Section 2.1) is 1.0Myr for $M_{\text{IMBH}} = 10^3 M_{\odot}$ and $M_{\text{BH}} = 60 M_{\odot}$. Since we imposed that only the binaries with $t_{\text{GW}} < 1.0\text{Myr}$ are merged in the simulation (see Section 2.1), most of our data points are located below this line, implying shorter merger timescales than 1.0Myr. The *right panel* shows the distribution of the mass of the secondary, M_{BH} , in the IMRI event, illustrating that more massive BHs are likely to merge with the IMBH. See Section 4.2 for more information.

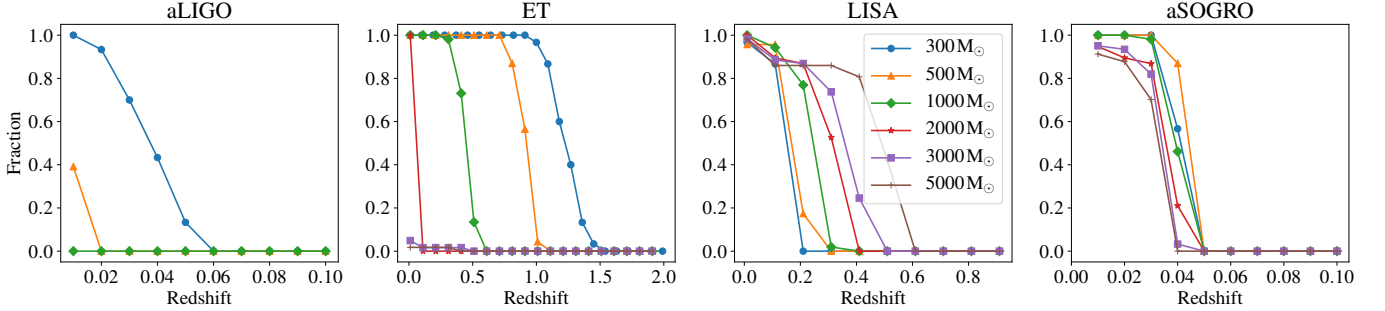


Figure 14. The fraction of IMRIs detectable ($S/N > 8$) by four observational instruments (aLIGO, ET, and LISA, and aSOGRO, from *left to right*) as a function of redshift, for IMBH masses, M_{IMBH} , from 300 to $5000 M_{\odot}$. The detectable redshift range varies significantly with the type of GW telescopes used. aLIGO is capable of detecting very close GW sources at $z \lesssim 0.06$ only for $M_{\text{IMBH}} = 300 M_{\odot}$. In contrast, ET can potentially detect some IMRIs up to $z \sim 1.5$. Note that the maximum redshift of detection (“horizon redshift”) sharply decreases as M_{IMBH} increases. LISA can detect IMRIs up to $z \sim 0.5$. Unlike ET, the maximum redshift of detection increases as M_{IMBH} increases. aSOGRO can detect the wide mass range of the IMRIs up to $z \sim 0.04$. The plot for DECIGO is omitted, as it can detect all IMRI events across the entire range of redshifts and masses considered in this study. See Section 5.1 for more information.

IMRIs including $M_{\text{IMBH}} \gtrsim 2000 M_{\odot}$ than ET. Meanwhile, aSOGRO’s horizon redshift is confined within the local universe $z \lesssim 0.05$. Although its detection range diminishes for higher mass IMBHs, DECIGO can detect IMRI events occurring at redshifts as high as $z \sim 10$.

In conclusion, both aLIGO and DECIGO may serve as a local probe for low-mass IMBHs, but aSOGRO covers a broader mass range. Meanwhile, ET and LISA can extend the cosmic volume under our detection up to $z \sim 0.5 - 1.0$, complementing each other in their detection capabilities across different mass ranges. Lastly, DECIGO can push the observational limits beyond $z \sim 10$ across all mass ranges.

5.2. IMRI Detection Rates By GW Observatories

We now estimate the IMRI detection rates by three different GW observatories, employing the GC number density as discussed in Section 2.3. In this work, the distribution of half-mass velocity dispersions, σ_{hm} , of GCs is derived from

$$\frac{dv_{\text{GC}}}{d\sigma_{\text{hm}}} = \frac{dv_{\text{GC}}}{dM_{\text{GC}}} \frac{dM_{\text{GC}}}{d\sigma_{\text{hm}}}. \quad (14)$$

Here, we use the relation $\sigma_{\text{hm}} = \sqrt{GM_{\text{GC}}/6R_{\text{hm}}}$ to estimate velocity dispersion, assuming a typical GC size of $R_{\text{hm}} \sim 2.5\text{pc}$, consistent with observations of GCs in the Milky Way (Portegies Zwart et al. 2010; Shin et al. 2013).

Combining and integrating Eqs.(6), (13) and (14) yields the expected IMRI detection rates per unit comoving volume at each redshift. Figure 16 shows the resulting detection rates for two natal kick scenarios (see Section 2.3). In both scenarios, all observatories except for aLIGO have the rate \sim a few

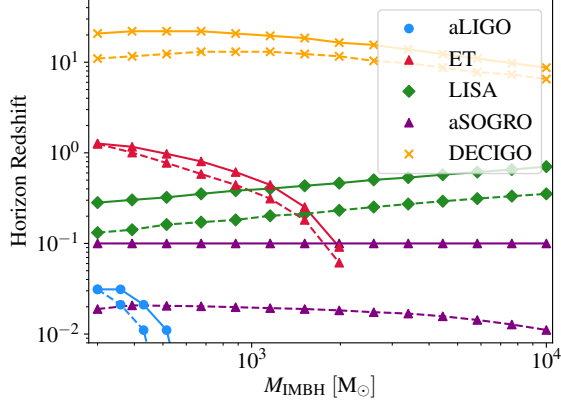


Figure 15. The horizon redshift as a function of the IMBH mass for each GW observatory. We assume that the secondary in the binary is a SBH of mass $10M_{\odot}$ (dashed line) and $60M_{\odot}$ (solid line), and that the eccentricities range from $e = 0.999$ to 0.99999 at 1 Myr before the merger. The figure shows that aLIGO can only detect IMRIs involving $M_{\text{IMBH}} \lesssim 500M_{\odot}$ at $z \lesssim 0.06$. ET has a significantly better capability for detecting these lower-mass IMBHs than aLIGO. However, there is a dramatic kink at $M_{\text{IMBH}} = 2000M_{\odot}$, meaning that ET is effective at detecting IMRIs involving IMBHs only with masses $M_{\text{IMBH}} \lesssim 2000$. Conversely, LISA and aSOGRO are capable of detecting IMBHs across all mass ranges in our analysis. However, LISA’s horizon redshift grows from $z \sim 0.2$ to $z \sim 0.5$ with M_{IMBH} increased, while aSOGRO’s is limited within $z \lesssim 0.05$. DECIGO possesses the widest detection range among the five observatories in our study. Ideally, it would detect all IMRIs from the entire universe. See Section 5.1 for more information.

$\times 10^{-8} \text{cMpc}^{-3} \text{yr}^{-1}$ at $z \lesssim 0.3$. First of all, its detection range encompasses the entire history of IMRI mergers, since DECIGO may cover all events up to a redshift $\lesssim 10$. LISA can detect some IMRIs up to the $z \lesssim 0.5$, while ET’s detection range extends slightly farther, up to $z \lesssim 1.0$. Despite their similar detection rates at $z < 0.3$, it is important to note that they are complementary in terms of the mass spectrum they can observe (see Figure 15 and Section 5.1).

Meanwhile, aLIGO and aSOGRO have much narrower detection ranges ($z \lesssim 0.06$); However, aLIGO exhibits a remarkably lower detection rate per unit comoving volume of $\lesssim 2 \times 10^{-9} \text{cMpc}^{-3} \text{yr}^{-1}$ compared to aSOGRO. This gap can be attributed to aLIGO’s limited detectable mass range even in the optimistic scenario with low natal kicks. In the pessimistic-case scenario in which many lower-mass IMBHs are ejected due to strong natal kicks, aLIGO will barely detect any IMRIs, even in very close proximity ($z < 0.01$). Figure 16 illustrates that, for some GW telescopes, the IMRI detection rate can be susceptible to the intensity of natal kicks assumed in our model.

By integrating the above results up to the horizon redshift, we derive the final conclusions of our study — that is the IMRI detection rates per year for different GW telescopes under two scenarios of BH natal kicks. The detection rate for

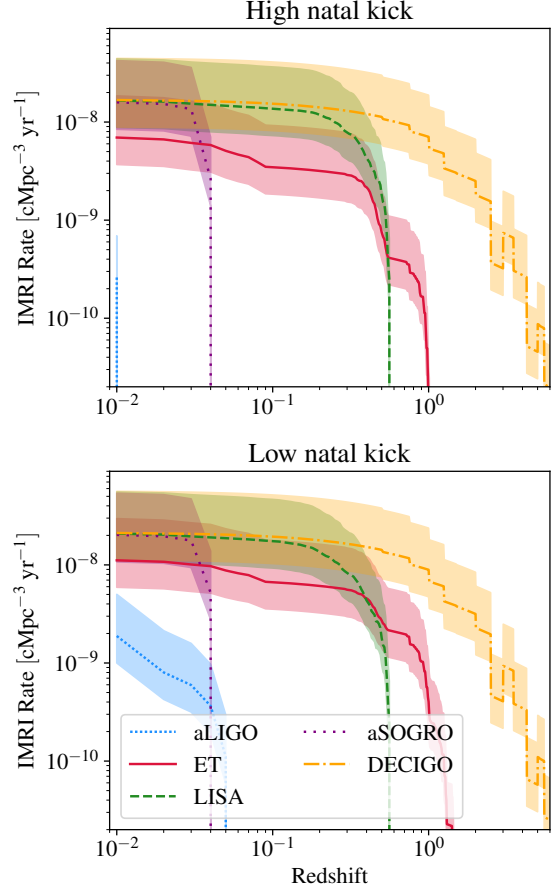


Figure 16. The prospect of IMRI detection rates per unit comoving volume at each redshift for aLIGO (densely-dotted blue line), ET (solid red line), LISA (dashed green line), aSOGRO (loosely-dotted purple line), and DECIGO (dash-dotted yellow line) under scenarios of high (top) and low (bottom) natal kicks (Section 2.3). The shaded region represents the range of detection rates corresponding to varying GC number densities, $n_{\text{GC}} = 0.77 - 3.77 \text{Mpc}^{-3}$ (Section 2.3). See Section 5.2 for more information.

aLIGO is found as

$$\Gamma_{\text{det, aLIGO}} \sim 1.1 \times 10^{-4} - 0.02 \text{yr}^{-1} \left(\frac{n_{\text{GC}, z=0}}{1.4 \text{Mpc}^{-3}} \right), \quad (15)$$

where we include the dependency on $n_{\text{GC}, z=0}$ in the formula. The aLIGO mainly targets low-mass IMBHs which are vulnerable to the recoil kick in general (Heggie 1975; Antonini & Rasio 2016; Arca Sedda et al. 2023). This makes it challenging to constrain the detection frequencies for IMBHs with $M_{\text{IMBH}} < 10^3 M_{\odot}$. In extreme cases, these IMBHs may be completely ejected from their host GCs during evolution. This uncertainty is reflected in Table 1 of Askar et al. (2022), which shows the highest variance in the retention of low-mass IMBHs. In summary, our results indicate that aLIGO will likely detect very few IMBHs, even under the most optimistic assumptions.

Meanwhile, the detection rate of upcoming GW observatories will significantly improve the chance of IMRI detection. The detection rate of the rest of GW observatories are as follows. The rate of ET is estimated as

$$\Gamma_{\text{det,ET}} \sim 101 - 355 \text{ yr}^{-1} \left(\frac{n_{\text{GC},z=0}}{1.4 \text{ Mpc}^{-3}} \right), \quad (16)$$

offering ample chances of IMRI detection for $M_{\text{IMBH}} \lesssim 10^3 M_{\odot}$. The detection rate of LISA is

$$\Gamma_{\text{det,LISA}} \sim 186 - 200 \text{ yr}^{-1} \left(\frac{n_{\text{GC},z=0}}{1.4 \text{ Mpc}^{-3}} \right). \quad (17)$$

LISA appears to be less affected by the natal kicks, as more massive IMBHs dominate its detectable IMRI populations (see Figure 15 and Section 5.1). The detection rate of aSOGRO is given as

$$\Gamma_{\text{det,aSOGRO}} \sim 0.24 - 0.34 \text{ yr}^{-1} \left(\frac{n_{\text{GC},z=0}}{1.4 \text{ Mpc}^{-3}} \right). \quad (18)$$

Lastly, the detection rate of DECIGO is estimated as

$$\Gamma_{\text{det,DECIGO}} \sim 3880 - 4890 \text{ yr}^{-1} \left(\frac{n_{\text{GC},z=0}}{1.4 \text{ Mpc}^{-3}} \right) \quad (19)$$

making it the most promising GW observatory for detecting IMRIs among those considered in this study.

According to our analyses, ET, LISA, and DECIGO are expected to provide robust detections of IMRIs, thereby greatly improving our ability to study the IMBH population over a wide range of masses and redshifts. Although aSOGRO exhibits a lower detection rate compared to other future observatories, it remains capable of detecting IMRI events within a practical observational timescale ($\sim 5 - 10$ yr).

5.3. Caveats In Our Analyses

In this section, we discuss the limitations of our study, focusing on the factors that are not considered in our analyses.

- Our simulations assume that the IMBH-BH binary tightens only via GW radiation. However, a binary may undergo multiple encounters with other stars or SBHs nearby; and, these “third” objects passing close to the center of mass of the hard binary can deform the binary configuration (Saslaw et al. 1974; Merritt & Milosavljević 2005). As a result, on average, the actual merger timescale could be shorter than our simulation results. More importantly, these interactions can significantly alter the characteristics of the observed GW signals. Also, the general relativistic effect such as the capture by gravitational capture (Quinlan & Shapiro 1989) is not included in our simulation. Given the rare frequency of the gravitational capture events, this would not affect our result significantly (See Appendix C).

- Our study also primarily focuses on the GW signals during the inspiral stage since it is the dominant source. However, despite its short duration, the merger and ringdown phases can also produce loud signals in some cases. Consequently, aLIGO and ET may have the potential to observe a broader mass spectrum than our predictions.
- In a realistic GW observation, multiple aspects can affect such as the Earth rotation (e.g., Isi et al. 2015). However, the SNR calculation utilizing Eq.(2) will not be significantly different from the precise measurement as an order of magnitude sense. Therefore, the actual IMRI detection rate will not be greatly far from our estimation.
- The time evolution of IMRI rates may depend on the formation mechanism of the IMBH. IMBHs can form through two distinct scenarios: the slow and fast scenarios (Giersz et al. 2015). In the slow scenario, an IMBH grows gradually over time by accreting stars and BHs, allowing IMRI events persists up to the present day. In contrast, in the fast scenario, where the IMBH forms via the runaway merger of massive stars, the majority of IMRI events are expected to occur within the first 5 Gyr, depleting the sources of IMRIs by low redshifts (Hong et al. 2020).
- The mass range of IMBHs is constrained to $M_{\text{IMBH}} < 10^4 M_{\odot}$ in our analysis. However, observatories such as LISA and DECIGO may be also sensitive to $M_{\text{IMBH}} > 10^4 M_{\odot}$. Consequently, the actual detection rates for these two observatories are likely to exceed the prediction of our analysis.
- The low-mass IMBHs are vulnerable to the GW recoil kicks from the IMBH-BH merger (González Prieto et al. 2022). The GW kick may eject most of the low-mass IMBH from the dense star clusters, and this would result in the decrease of the IMRI rate for IMRIs with ($M_{\text{IMBH}} < 10^3 M_{\odot}$). The impact of GW kick on the IMRI detection rate will be rather limited since detectors such as LISA and aSOGRO are sensitive to higher mass regimes. Meanwhile, ET and aLIGO may detect less frequently than our estimations although we already concluded that aLIGO would be less likely to detect any IMRIs in a practical timescale.
- The detailed evolution of the IMRI rate across cosmic time may exhibit significant variations depending on the assumptions on the GC formation and evolution history. For example, a semi-analytic model work of Fragione et al. (2018) accounts for the mass loss of GCs due to the galactic tidal field. Their study predicts

that at low redshift, the IMRI event rate falls within the range of $\sim 0.5 - 3 \text{ Gpc}^{-3} \text{ yr}^{-1}$. However, during the peak GC formation epoch, this rate increases as high as $\sim 100 \text{ Gpc}^{-3} \text{ yr}^{-1}$. In contrast, our simulations, which focus on short-term GC evolution, predict an order of magnitude higher IMRI rates than those found in (Fragione et al. 2018), while it declines at higher redshifts because of the decreasing GC number density.

6. SUMMARY AND CONCLUSION

Using a suite of direct N -body simulations we have studied the IMRI event rates, while varying the velocity dispersion of the embedding GCs and the mass of the central IMBHs. We have also explored the distribution of the orbital parameters of the simulated IMBH-BH binaries. Our simulation study thus provides a comprehensive overview of the IMRI statistics, namely, the event rates and the orbital properties (Section 4). With this information, we have estimated the detection rates of IMRI events involving IMBHs by the current and future ground-/space-based GW observatories (Section 5). Our main results are summarized as follows:

- The IMRI event rate typically falls in the range of $0.1 - 0.3 \text{ Myr}^{-1}$ for the IMBHs of mass $M_{\text{IMBH}} = 300 - 5000 M_{\odot}$. The IMRI event rate is influenced by both the velocity dispersion of the embedding GCs and the mass of the IMBH (Section 4.2).
- LISA can detect IMRIs involving IMBHs across a wide range of IMBH masses, with its horizon redshift increasing as M_{IMBH} increases. It can detect the majority of eccentric IMRIs in the local universe, and even some IMRIs with $M_{\text{IMBH}} = 5000 M_{\odot}$ up to $z \sim 0.5$. Although ET's detection capability is restricted to IMRIs with $M_{\text{IMBH}} \lesssim 2000 M_{\odot}$, it serves as a complementary instrument to LISA within this mass spectrum. DECIGO extends GW observational range beyond $z \sim 10$, covering the entire mass ranges considered in our analysis. In contrast, aSOGRO's horizon redshift is limited within the Milky Way's vicinity as aLIGO's (Section 5.1). Nevertheless, aSOGRO is capable of covering a broader mass spectrum than aLIGO.
- Integrating the above results in the redshift space, we derive the IMRI detection rate per year for three GW observatories: $\lesssim 0.04 \text{ yr}^{-1}$ for aLIGO, $\sim 101 - 355 \text{ yr}^{-1}$ for ET, $\sim 186 - 200 \text{ yr}^{-1}$ for LISA, $\sim 0.24 -$

0.34 yr^{-1} for aSOGRO, and $\sim 3880 - 4890 \text{ yr}^{-1}$ for DECIGO. This result can be affected by the (local) GC number density or the IMBH retention fraction (Section 5.2).

Our study provides a pipeline to investigate the IMRI detection rates for GW observatories, by utilizing direct N -body simulations on dense stellar systems. Our results demonstrates that the upcoming GW observatories will have several chance of observing the IMRIs. With the improved observational constraints in the future, such as the local GC density and BH natal kicks, our pipeline will provide a comprehensive perspective on the robust detection of IMBHs.

Other than the GW radiated from IMRIs explored in this study, there are several observable signals for IMBHs. One can be the optical flare from the tidal disruption of stars or white dwarfs by IMBHs (Strubbe & Quataert 2009). If detected, the IMBH-IMBH merger can be considerably manifest (Rasskazov et al. 2020). In addition, a hypervelocity star escaping from a star cluster can be another indirect evidence of the IMBH (Fragione & Gualandris 2019). We leave the study of providing a more realistic IMBH detection rate by considering all of these factors as our future project.

- 1 Seungjae Lee would like to thank Chan Park, and Boon
- 2 Kiat Oh for their kind and enlightening comments on the
- 3 early version of this manuscript. We are grateful to Han
- 4 Gil Choi who kindly introduced us a detailed background in-
- 5 formation on the GW detections. We also thank Sambaran
- 6 Banerjee, Francesco Maria Flammini Dotti and Kai Wu for
- 7 their insightful discussions and detailed comments on the N -
- 8 body simulations. Hyung Mok Lee was supported by Na-
- 9 tional Research Foundation of Korea (NRF) grant funded by
- 10 the Korea government (MSIT) (No. 2021M3F7A1082056).
- 11 Ji-hoon Kim's work was supported by the NRF grant
- 12 (No. 2022M3K3A1093827 and No. 2023R1A2C1003244).
- 13 His work was also supported by the Global-LAMP Pro-
- 14 gram of the NRF grant funded by the Ministry of Educa-
- 15 tion (No. RS-2023-00301976). His work was also sup-
- 16 ported by the National Institute of Supercomputing and Net-
- 17 work/Korea Institute of Science and Technology Informa-
- 18 tion with supercomputing resources including technical sup-
- 19 port, grants KSC-2021-CRE-0442, KSC-2022-CRE-0355
- 20 and KSC-2024-CRE-0232.

APPENDIX

A. HARDNESS OF THE BINARY

The hardness of an IMBH-BH binary can be quantified as $H = |E_b|/E_k$, where $E_b = -GM_{\text{IMBH}}M_{\text{BH}}/(2a)$ represents the binding energy of the binary, and $E_k = M_{\text{third}}v_{\text{third}}^2/2$ is the typical kinetic energy of surrounding stars and BHs. Here, M_{third} is the mass of an incoming third particle, and v is its velocity. Using the parameters $M_{\text{IMBH}} = 1000M_{\odot}$, $M_{\text{BH}} = 20M_{\odot}$, $a = 10\text{au}$, $M_{\text{third}} = 10M_{\odot}$, $v_{\text{third}} = 10\text{km s}^{-1}$ gives us $H \approx 1800$. Refer to Table 1 and Figure 13 for the choice of those parameters. This high hardness value indicates that the binary is sufficiently resistant to disruption from third-body encounters.

B. THE MULTI-BODY INTERACTION TIMESCALE

The timescale of encounters between an IMBH-BH binary and a third body can be estimated by

$$t_{\text{encounter}} = 1/(n\Sigma_b v) \quad (\text{B1})$$

where n is the number density of stars and SBHs in the region surrounding the binary, Σ_b is the cross-section of the binary, and v is the speed of the encountering object, or the velocity dispersion. Inserting $n = 10^5\text{pc}^{-3}$, $\Sigma_b = \pi R_b^2$, and $v = 7\text{km s}^{-1}$ gives us $t_{\text{encounter}} \approx 45\text{Myr}$ (See Table 1). Here, we choose the radius of the binary to be $R_b = 10^{-4}\text{pc}$ considering the merger criteria in our simulations. This result indicates that an IMBH-BH binary is unlikely to encounter a third-body within the GW merger timescale of 1 Myr assumed in our model.

C. THE GRAVITATIONAL CAPTURE TIMESCALE

When two black holes become close, gravitational radiation may dissipate most of the orbital kinetic energy, thus forming a binary. The timescale of the gravitational capture can be estimated in the similar manner as Equation B1:

$$t_{\text{DG}} = 1/(n\Sigma_{\text{GR,cap}} v) \quad (\text{C2})$$

where Σ_{DG} is the cross-section of the gravitational capture. Exploiting Equation (15) of Lee (1995), we estimate Σ_{DG} as follows:

$$\Sigma_{\text{DG,cap}} = 2\pi \left(\frac{85\pi}{6\sqrt{2}} \right)^{2/7} \frac{G^2 M_{\text{IMBH}}^{2/7} M_{\text{BH}}^{2/7} (M_{\text{IMBH}} + M_{\text{BH}})^{10/7}}{c^{10/7} v^{18/7}}. \quad (\text{C3})$$

Substituting $n = 10^5\text{pc}^{-3}$, $M_{\text{IMBH}} = 10^3 M_{\odot}$, $M_{\text{BH}} = 10M_{\odot}$, and $v = 15\text{km s}^{-1}$ into Equation C2 and ?? yields a direct merger timescale of $t_{\text{DG}} \approx 550\text{Myr}$, corresponding to a merger rate of $\lesssim 0.002\text{Myr}^{-1}$. This result demonstrates that the direct gravitational capture event would be rarer than IMRIs driven by gravitational wave dissipation.

D. DETAILS OF THE N -BODY UNITS

All the N -body simulations use dimensionless units (Aarseth 2003). For a star cluster with initial total particle number N , and the mean particle mass, \bar{M} in M_{\odot} , and equilibrium virial radius, \bar{R} in parsec, are set to be unity with the total energy $E_0 = -0.25$ for bound systems. Then the physical unit of velocity and time can be expressed as

$$\bar{V} = 6.557 \times 10^{-2} \left(\frac{N\bar{M}}{\bar{R}} \right) \text{km s}^{-1}, \quad (\text{D4})$$

$$\bar{T} = 14.94 \left(\frac{\bar{R}^3}{N\bar{M}} \right)^{1/2} \text{Myr}. \quad (\text{D5})$$

The virial radius of the Plummer model, which is adopted in our experiments, is approximately estimated by $\bar{R} = 1.3R_{\text{hm}}$

E. THE SCHECHTER FUNCTION

The number density of the galaxies can be obtained by integrating the Schechter (1976) function. The Schechter function for the number densities of galaxies is given by

$$\phi(\bar{M}) = \phi^* \ln(10) \left[10^{b(\bar{M}-M^*)} \right]^{(1+\alpha)} \exp\left(-10^{b(\bar{M}-M^*)}\right), \quad (\text{E6})$$

where the parameters ϕ^* , α , M_* , and M^* are from Table 1 of Conselice et al. (2016) and redshift-dependent, and $\bar{M} = \log M_*$. The total number densities of the galaxies at a given redshift can be estimated by integrating this function as

$$\phi_{\Gamma}(z) = \int_{\bar{M}_1}^{\bar{M}_2} \phi(\bar{M}, z) d\bar{M}, \quad (\text{E7})$$

whose integrated form can be well approximated by

$$\phi_T(z) \approx \frac{-\phi^* 10^{(\alpha+1)(M_2-M^*)}}{\alpha+1}. \quad (\text{E8})$$

We also assume that the stellar masses of galaxies are all identical to $6 \times 10^{10} M_\odot$. The total number of galaxies at $z < z_0$ can be given by the integral

$$N_{\text{tot}} = \int_0^{t_0} \int_0^{4\pi} D_H \frac{(1+z)^2 D_A^2}{E(z)} \phi_T(t) d\Omega dt, \quad (\text{E9})$$

where D_A is the angular size distance, $D_H = c/H_0$, and $E(z) = (\Omega_M(1+z)^3 + \Omega_\lambda)^{1/2}$.

F. EVOLUTION OF THE IMBH-BH BINARY

The orbit-averaged evolution of the semi-major axis a and eccentricity e is given by (Peters 1964):

$$\left\langle \frac{da}{dt} \right\rangle = -\frac{64 G^3 M_1 M_2 (M_1 + M_2)}{5 c^5 a^3 (1-e^2)^{7/2}} \left(1 + \frac{73}{24} e^2 + \frac{37}{96} e^4 \right) \quad (\text{F10})$$

and

$$\left\langle \frac{de}{dt} \right\rangle = -\frac{304 G^3 M_1 M_2 (M_1 + M_2)}{15 c^5 a^4 (1-e^2)^{5/2}} \left(1 + \frac{121}{304} e^2 \right). \quad (\text{F11})$$

Additionally, the time-averaged energy emission rate is

$$\left\langle \frac{dE}{dt} \right\rangle = -\frac{32 G^4 M_1^2 M_2^2 (M_1 + M_2)}{5 c^5 a^5 (1-e^2)^{7/2}} \left(1 + \frac{73}{24} e^2 + \frac{37}{96} e^4 \right), \quad (\text{F12})$$

while their merger timescale is estimated using Eq.(1).

Following Eqs.(19) - (20) of Peters & Mathews (1963), the power radiated through the n -th harmonic can be computed as

$$\dot{E}_n = \frac{32 G^4 M_1^2 M_2^2 (M_1 + M_2)}{5 c^5 a^5} g(n, e), \quad (\text{F13})$$

where

$$g(n, e) = \frac{n^4}{32} \left\{ \left[J_{n-2}(ne) - 2eJ_{n-1}(ne) + \frac{2}{n}J_n(ne) \right. \right. \\ \left. \left. + 2eJ_{n+1}(ne) - J_{n+2}(ne) \right]^2 + (1-e^2) [J_{n-2}(ne) \right. \\ \left. - 2J_n(ne) + J_{n+2}(ne) \right]^2 + \frac{4}{3n^2} [J_n(ne)]^2 \right\}, \quad (\text{F14})$$

and J_n are Bessel functions of the first kind.

G. NUMBER DENSITY OF GLOBULAR CLUSTERS

The total stellar mass contained in a GC can be approximated as

$$M_{\text{tot,GC}} = S_M M_{G_*} \quad (\text{G15})$$

with the specific mass $S_M \approx 0.001 - 0.003$ and the total bulge stellar mass M_{G_*} (Peng et al. 2008; Harris et al. 2013). Then we can obtain the GC number density by the integral

$$n_{\text{GC}}(z) = \int_{\bar{M}_1}^{\bar{M}_2} \phi(\bar{M}, z) N_{\text{GCs}}(\bar{M}) d\bar{M}, \quad (\text{G16})$$

where the number of GCs in a galaxy, $N_{\text{GCs}}(\bar{M}) = 10^{-4} M_* / \langle M_{\text{GC}} \rangle$.

H. THE SENSITIVITY CURVES OF DETECTORS

We model the sensitivity curves of the five detectors: aLIGO,⁴ ET,⁵ LISA, aSOGRO, and DECIGO. The sensitivity of LISA is estimated using Eq.(13) of Robson et al. (2019), as

$$S_{h,\text{LISA}}(f) = \frac{10}{3L_{\text{LISA}}^2} \left(P_{\text{OMS}}(f) + \frac{4P_{\text{acc}}(f)}{(2\pi f)^4} \right) \times \left(1 + \frac{3}{5} \left(\frac{f}{f_*} \right)^2 \right) + S_c(f), \quad (\text{H17})$$

where $L_{\text{LISA}} = 2.5 \times 10^{11}$ cm is the arm length of LISA, $f_* = 19.09$ mHz, $P_{\text{OMS}}(f)$ is the optical metrology noise, $P_{\text{acc}}(f)$ is the acceleration noise, and $S_c(f)$ is the confusion noise. For details of this expression, we refer the interested readers to Robson et al. (2019). In the present study, we ignore the contribution of the confusion noise.

The sensitivity of aSOGRO is drawn based on the Eq.(13) and Table.(1) of Bae et al. (2024), as

$$S_{h,\text{SOGRO}}(f) = \frac{16}{M_{\text{TM}} L_{\text{aSOGRO}}^2 \omega^4} \times \left[\frac{k_B T \omega_D}{Q_D} + \frac{|\omega^2 - \omega_D^2|}{\omega_p} \left(1 + \frac{1}{\beta^2} \right)^{1/2} k_B T_N \right]. \quad (\text{H18})$$

with $\omega = 2\pi f$ is the angular frequency, k_B is the Boltzmann constant, $M_{\text{TM}} = 5000$ kg is the mass of the individual freely moving test masses, and $L_{\text{aSOGRO}} = 50$ m is the arm length of aSOGRO, respectively; $T = 0.1$ K is the Antenna temperature; $Q_D = 10^8$ and $\omega_D = 2\pi \times 10^{-2}$ Hz is the angular resonance frequency and quality factor of differential mode (DM); $\omega_p = 2\pi \times 50$ kHz is the pump (angular) frequency; $T_N \equiv 5\hbar\omega_p/k_B$ is the noise temperature. The energy coupling constant β is computed by

$$\beta = \frac{2CE_p^2 Q_p}{M_{\text{TM}} |\omega^2 - \omega_D^2|} \frac{1}{\sqrt{1 + (2Q_p \omega / \omega_p)^2}} \quad (\text{H19})$$

where $C = 4 \times 10^{-9}$ F is the equilibrium value of each sensing capacitor, $E_p = 5 \times 10^5$ V m⁻¹ is the amplitude of the driving electric at ω_p , and $Q_p = 10^6$ is platform quality factor.

The sensitivity curve of DECIGO is given by the Eq.(5) of (Yagi & Seto 2011), as

$$S_{h,\text{DECIGO}}(f) = 6.53 \times 10^{-49} \left[1 + \left(\frac{f}{7.36 \text{ Hz}} \right)^2 \right] + 4.45 \times 10^{-51} \left(\frac{f}{1 \text{ Hz}} \right)^{-4} \left[1 + \left(\frac{f}{7.36 \text{ Hz}} \right)^2 \right]^{-1} + 4.94 \times 10^{-52} \left(\frac{f}{1 \text{ Hz}} \right)^{-4} \text{ Hz}. \quad (\text{H20})$$

REFERENCES

- Aarseth, S. J. 1999, PASP, 111, 1333, doi: [10.1086/316455](https://doi.org/10.1086/316455)
- . 2003, Gravitational N-Body Simulations
- Ahmad, A., & Cohen, L. 1973, Journal of Computational Physics, 12, 389, doi: [10.1016/0021-9991\(73\)90160-5](https://doi.org/10.1016/0021-9991(73)90160-5)
- ⁴ <https://dcc.ligo.org/cgi-bin/DocDB/DocumentDatabase>
- ⁵ Hild et al. (2011)
- Amaro-Seoane, P. 2018, PhRvD, 98, 063018, doi: [10.1103/PhysRevD.98.063018](https://doi.org/10.1103/PhysRevD.98.063018)
- Antonini, F., Barausse, E., & Silk, J. 2015, ApJ, 812, 72, doi: [10.1088/0004-637X/812/1/72](https://doi.org/10.1088/0004-637X/812/1/72)
- Antonini, F., & Rasio, F. A. 2016, ApJ, 831, 187, doi: [10.3847/0004-637X/831/2/187](https://doi.org/10.3847/0004-637X/831/2/187)
- Arca-Sedda, M. 2016, MNRAS, 455, 35, doi: [10.1093/mnras/stv2265](https://doi.org/10.1093/mnras/stv2265)

- Arca Sedda, M., Amaro Seoane, P., & Chen, X. 2021, *A&A*, 652, A54, doi: [10.1051/0004-6361/202037785](https://doi.org/10.1051/0004-6361/202037785)
- Arca Sedda, M., Kamlah, A. W. H., Spurzem, R., et al. 2023, *MNRAS*, 526, 429, doi: [10.1093/mnras/stad2292](https://doi.org/10.1093/mnras/stad2292)
- Askar, A., Davies, M. B., & Church, R. P. 2022, *MNRAS*, 511, 2631, doi: [10.1093/mnras/stab3741](https://doi.org/10.1093/mnras/stab3741)
- Askar, A., Szkudlarek, M., Gondek-Rosińska, D., Giersz, M., & Bulik, T. 2017, *MNRAS*, 464, L36, doi: [10.1093/mnras/lslw177](https://doi.org/10.1093/mnras/lslw177)
- Bacon, R., Emsellem, E., Monnet, G., & Nieto, J. L. 1994, *A&A*, 281, 691, doi: [10.48550/arXiv.astro-ph/9309008](https://doi.org/10.48550/arXiv.astro-ph/9309008)
- Bae, Y.-B., Park, C., Son, E. J., et al. 2024, *Progress of Theoretical and Experimental Physics*, 2024, 053E01, doi: [10.1093/ptep/ptae045](https://doi.org/10.1093/ptep/ptae045)
- Bahcall, J. N., & Wolf, R. A. 1976, *ApJ*, 209, 214, doi: [10.1086/154711](https://doi.org/10.1086/154711)
- Barack, L., & Cutler, C. 2004, *PhRvD*, 69, 082005, doi: [10.1103/PhysRevD.69.082005](https://doi.org/10.1103/PhysRevD.69.082005)
- Baumgardt, H. 2017, *MNRAS*, 464, 2174, doi: [10.1093/mnras/stw2488](https://doi.org/10.1093/mnras/stw2488)
- Baumgardt, H., Makino, J., & Ebisuzaki, T. 2004a, *ApJ*, 613, 1143, doi: [10.1086/423299](https://doi.org/10.1086/423299)
- . 2004b, *ApJ*, 613, 1133, doi: [10.1086/423298](https://doi.org/10.1086/423298)
- Begelman, M. C., & Rees, M. J. 1978, *MNRAS*, 185, 847, doi: [10.1093/mnras/185.4.847](https://doi.org/10.1093/mnras/185.4.847)
- Belczynski, K., Kalogera, V., & Bulik, T. 2002, *ApJ*, 572, 407, doi: [10.1086/340304](https://doi.org/10.1086/340304)
- Brown, D. A., Brink, J., Fang, H., et al. 2007, *PhRvL*, 99, 201102, doi: [10.1103/PhysRevLett.99.201102](https://doi.org/10.1103/PhysRevLett.99.201102)
- Caputi, K. I., Cirasuolo, M., Dunlop, J. S., et al. 2011, *MNRAS*, 413, 162, doi: [10.1111/j.1365-2966.2010.18118.x](https://doi.org/10.1111/j.1365-2966.2010.18118.x)
- Cohn, H. 1980, *ApJ*, 242, 765, doi: [10.1086/158511](https://doi.org/10.1086/158511)
- Conselice, C. J., Wilkinson, A., Duncan, K., & Mortlock, A. 2016, *ApJ*, 830, 83, doi: [10.3847/0004-637X/830/2/83](https://doi.org/10.3847/0004-637X/830/2/83)
- den Brok, M., Seth, A. C., Barth, A. J., et al. 2015, *ApJ*, 809, 101, doi: [10.1088/0004-637X/809/1/101](https://doi.org/10.1088/0004-637X/809/1/101)
- Finn, L. S., & Thorne, K. S. 2000, *PhRvD*, 62, 124021, doi: [10.1103/PhysRevD.62.124021](https://doi.org/10.1103/PhysRevD.62.124021)
- Fragione, G., & Gualandris, A. 2019, *MNRAS*, 489, 4543, doi: [10.1093/mnras/stz2451](https://doi.org/10.1093/mnras/stz2451)
- Fragione, G., Leigh, N. W. C., Ginsburg, I., & Kocsis, B. 2018, *ApJ*, 867, 119, doi: [10.3847/1538-4357/aae486](https://doi.org/10.3847/1538-4357/aae486)
- Fragione, G., Loeb, A., Kocsis, B., & Rasio, F. A. 2022, *ApJ*, 933, 170, doi: [10.3847/1538-4357/ac75d0](https://doi.org/10.3847/1538-4357/ac75d0)
- Freitag, M., Amaro-Seoane, P., & Kalogera, V. 2006a, in *Journal of Physics Conference Series*, Vol. 54, *Journal of Physics Conference Series*, ed. R. Schödel, G. C. Bower, M. P. Muno, S. Nayakshin, & T. Ott (IOP), 252–258, doi: [10.1088/1742-6596/54/1/040](https://doi.org/10.1088/1742-6596/54/1/040)
- Freitag, M., Gürkan, M. A., & Rasio, F. A. 2006b, *MNRAS*, 368, 141, doi: [10.1111/j.1365-2966.2006.10096.x](https://doi.org/10.1111/j.1365-2966.2006.10096.x)
- Freitag, M., Rasio, F. A., & Baumgardt, H. 2006c, *MNRAS*, 368, 121, doi: [10.1111/j.1365-2966.2006.10095.x](https://doi.org/10.1111/j.1365-2966.2006.10095.x)
- Gair, J. R., Mandel, I., Miller, M. C., & Volonteri, M. 2011, *General Relativity and Gravitation*, 43, 485, doi: [10.1007/s10714-010-1104-3](https://doi.org/10.1007/s10714-010-1104-3)
- Gieles, M. 2009, *MNRAS*, 394, 2113, doi: [10.1111/j.1365-2966.2009.14473.x](https://doi.org/10.1111/j.1365-2966.2009.14473.x)
- Giersz, M., Leigh, N., Hypki, A., Lützgendorf, N., & Askar, A. 2015, *MNRAS*, 454, 3150, doi: [10.1093/mnras/stv2162](https://doi.org/10.1093/mnras/stv2162)
- González, E., Kremer, K., Chatterjee, S., et al. 2021, *ApJL*, 908, L29, doi: [10.3847/2041-8213/abdf5b](https://doi.org/10.3847/2041-8213/abdf5b)
- González Prieto, E., Kremer, K., Fragione, G., et al. 2022, *ApJ*, 940, 131, doi: [10.3847/1538-4357/ac9b0f](https://doi.org/10.3847/1538-4357/ac9b0f)
- Greene, J. E., Strader, J., & Ho, L. C. 2020, *ARA&A*, 58, 257, doi: [10.1146/annurev-astro-032620-021835](https://doi.org/10.1146/annurev-astro-032620-021835)
- Gürkan, M. A., Freitag, M., & Rasio, F. A. 2004, *ApJ*, 604, 632, doi: [10.1086/381968](https://doi.org/10.1086/381968)
- Häberle, M., Neumayer, N., Seth, A., et al. 2024, *Nature*, 631, 285, doi: [10.1038/s41586-024-07511-z](https://doi.org/10.1038/s41586-024-07511-z)
- Harris, W. E., Harris, G. L. H., & Alessi, M. 2013, *ApJ*, 772, 82, doi: [10.1088/0004-637X/772/2/82](https://doi.org/10.1088/0004-637X/772/2/82)
- Heggie, D. C. 1975, *MNRAS*, 173, 729, doi: [10.1093/mnras/173.3.729](https://doi.org/10.1093/mnras/173.3.729)
- Hild, S., Abernathy, M., Acernese, F., et al. 2011, *Classical and Quantum Gravity*, 28, 094013, doi: [10.1088/0264-9381/28/9/094013](https://doi.org/10.1088/0264-9381/28/9/094013)
- Hobbs, G., Lorimer, D. R., Lyne, A. G., & Kramer, M. 2005, *MNRAS*, 360, 974, doi: [10.1111/j.1365-2966.2005.09087.x](https://doi.org/10.1111/j.1365-2966.2005.09087.x)
- Hong, J., Askar, A., Giersz, M., Hypki, A., & Yoon, S.-J. 2020, *MNRAS*, 498, 4287, doi: [10.1093/mnras/staa2677](https://doi.org/10.1093/mnras/staa2677)
- Hong, J., & Lee, H. M. 2015, *MNRAS*, 448, 754, doi: [10.1093/mnras/stv035](https://doi.org/10.1093/mnras/stv035)
- Hut, P., Makino, J., & McMillan, S. 1995, *ApJL*, 443, L93, doi: [10.1086/187844](https://doi.org/10.1086/187844)
- Iorio, G., Mapelli, M., Costa, G., et al. 2023, *MNRAS*, 524, 426, doi: [10.1093/mnras/stad1630](https://doi.org/10.1093/mnras/stad1630)
- Isi, M., Weinstein, A. J., Mead, C., & Pitkin, M. 2015, *PhRvD*, 91, 082002, doi: [10.1103/PhysRevD.91.082002](https://doi.org/10.1103/PhysRevD.91.082002)
- Kamlah, A. W. H., Leveque, A., Spurzem, R., et al. 2022, *MNRAS*, 511, 4060, doi: [10.1093/mnras/stab3748](https://doi.org/10.1093/mnras/stab3748)
- Kormendy, J., & Ho, L. C. 2013, *ARA&A*, 51, 511, doi: [10.1146/annurev-astro-082708-101811](https://doi.org/10.1146/annurev-astro-082708-101811)
- Kroupa, P. 2001, *MNRAS*, 322, 231, doi: [10.1046/j.1365-8711.2001.04022.x](https://doi.org/10.1046/j.1365-8711.2001.04022.x)
- Küpfer, A. H. W., Maschberger, T., Kroupa, P., & Baumgardt, H. 2011, *MNRAS*, 417, 2300, doi: [10.1111/j.1365-2966.2011.19412.x](https://doi.org/10.1111/j.1365-2966.2011.19412.x)
- Kustaanheimo, P., SCHINZEL, A., DAVENPORT, H., & STIEFEL, E. 1965, *Journal für die reine und angewandte Mathematik*, 1965, 204, doi: [doi:10.1515/crll.1965.218.204](https://doi.org/10.1515/crll.1965.218.204)

- Lee, H. M. 1995, *MNRAS*, 272, 605, doi: [10.1093/mnras/272.3.605](https://doi.org/10.1093/mnras/272.3.605)
- Lin, D., Strader, J., Carrasco, E. R., et al. 2018, *Nature Astronomy*, 2, 656, doi: [10.1038/s41550-018-0493-1](https://doi.org/10.1038/s41550-018-0493-1)
- Mandel, I., Brown, D. A., Gair, J. R., & Miller, M. C. 2008, *ApJ*, 681, 1431, doi: [10.1086/588246](https://doi.org/10.1086/588246)
- Mapelli, M. 2016, *MNRAS*, 459, 3432, doi: [10.1093/mnras/stw869](https://doi.org/10.1093/mnras/stw869)
- McMillan, S. L. W. 1986, in *The Use of Supercomputers in Stellar Dynamics*, ed. P. Hut & S. L. W. McMillan (Berlin, Heidelberg: Springer Berlin Heidelberg), 156–161
- Merritt, D., & Milosavljević, M. 2005, *Living Reviews in Relativity*, 8, 8, doi: [10.12942/lrr-2005-8](https://doi.org/10.12942/lrr-2005-8)
- Mikkola, S., & Merritt, D. 2008, *AJ*, 135, 2398, doi: [10.1088/0004-6256/135/6/2398](https://doi.org/10.1088/0004-6256/135/6/2398)
- Mikkola, S., & Tanikawa, K. 1999, *MNRAS*, 310, 745, doi: [10.1046/j.1365-8711.1999.02982.x](https://doi.org/10.1046/j.1365-8711.1999.02982.x)
- Neumayer, N., Seth, A., & Böker, T. 2020, *A&A Rv*, 28, 4, doi: [10.1007/s00159-020-00125-0](https://doi.org/10.1007/s00159-020-00125-0)
- Nguyen, D. D., Seth, A. C., Neumayer, N., et al. 2018, *ApJ*, 858, 118, doi: [10.3847/1538-4357/aabe28](https://doi.org/10.3847/1538-4357/aabe28)
- . 2019, *ApJ*, 872, 104, doi: [10.3847/1538-4357/aafe7a](https://doi.org/10.3847/1538-4357/aafe7a)
- Nitadori, K., & Aarseth, S. J. 2012, *MNRAS*, 424, 545, doi: [10.1111/j.1365-2966.2012.21227.x](https://doi.org/10.1111/j.1365-2966.2012.21227.x)
- Noyola, E., Gebhardt, K., Kissler-Patig, M., et al. 2010, *ApJL*, 719, L60, doi: [10.1088/2041-8205/719/1/L60](https://doi.org/10.1088/2041-8205/719/1/L60)
- Paik, H. J., Griggs, C. E., Vol Moody, M., et al. 2016, *Classical and Quantum Gravity*, 33, 075003, doi: [10.1088/0264-9381/33/7/075003](https://doi.org/10.1088/0264-9381/33/7/075003)
- Peng, E. W., Jordán, A., Côté, P., et al. 2008, *ApJ*, 681, 197, doi: [10.1086/587951](https://doi.org/10.1086/587951)
- Peters, P. C. 1964, *Physical Review*, 136, 1224, doi: [10.1103/PhysRev.136.B1224](https://doi.org/10.1103/PhysRev.136.B1224)
- Peters, P. C., & Mathews, J. 1963, *Physical Review*, 131, 435, doi: [10.1103/PhysRev.131.435](https://doi.org/10.1103/PhysRev.131.435)
- Portegies Zwart, S., & McMillan, S. 1999, arXiv e-prints, astro, doi: [10.48550/arXiv.astro-ph/9912022](https://doi.org/10.48550/arXiv.astro-ph/9912022)
- Portegies Zwart, S. F., & McMillan, S. L. W. 2002, *ApJ*, 576, 899, doi: [10.1086/341798](https://doi.org/10.1086/341798)
- Portegies Zwart, S. F., McMillan, S. L. W., & Gieles, M. 2010, *ARA&A*, 48, 431, doi: [10.1146/annurev-astro-081309-130834](https://doi.org/10.1146/annurev-astro-081309-130834)
- Quinlan, G. D., & Shapiro, S. L. 1989, *ApJ*, 343, 725, doi: [10.1086/167745](https://doi.org/10.1086/167745)
- Rasskazov, A., Fragione, G., & Kocsis, B. 2020, *ApJ*, 899, 149, doi: [10.3847/1538-4357/aba2f4](https://doi.org/10.3847/1538-4357/aba2f4)
- Rees, M. J. 1988, *Nature*, 333, 523, doi: [10.1038/333523a0](https://doi.org/10.1038/333523a0)
- Rizzuto, F. P., Naab, T., Spurzem, R., et al. 2021, *MNRAS*, 501, 5257, doi: [10.1093/mnras/staa3634](https://doi.org/10.1093/mnras/staa3634)
- Robson, T., Cornish, N. J., & Liu, C. 2019, *Classical and Quantum Gravity*, 36, 105011, doi: [10.1088/1361-6382/ab1101](https://doi.org/10.1088/1361-6382/ab1101)
- Rodriguez, C. L., Morscher, M., Pattabiraman, B., et al. 2015, *PhRvL*, 115, 051101, doi: [10.1103/PhysRevLett.115.051101](https://doi.org/10.1103/PhysRevLett.115.051101)
- Saslaw, W. C., Valtonen, M. J., & Aarseth, S. J. 1974, *ApJ*, 190, 253, doi: [10.1086/152870](https://doi.org/10.1086/152870)
- Sathyaprakash, B., Abernathy, M., Acernese, F., et al. 2012, *Classical and Quantum Gravity*, 29, 124013, doi: [10.1088/0264-9381/29/12/124013](https://doi.org/10.1088/0264-9381/29/12/124013)
- Schechter, P. 1976, *ApJ*, 203, 297, doi: [10.1086/154079](https://doi.org/10.1086/154079)
- Schödel, R., Merritt, D., & Eckart, A. 2009, *A&A*, 502, 91, doi: [10.1051/0004-6361/200810922](https://doi.org/10.1051/0004-6361/200810922)
- Shin, J., Kim, S. S., Yoon, S.-J., & Kim, J. 2013, *ApJ*, 762, 135, doi: [10.1088/0004-637X/762/2/135](https://doi.org/10.1088/0004-637X/762/2/135)
- Sigurdsson, S., Hernquist, L., & Quinlan, G. D. 1995, *ApJ*, 446, 75, doi: [10.1086/175769](https://doi.org/10.1086/175769)
- Song, M., Finkelstein, S. L., Ashby, M. L. N., et al. 2016, *ApJ*, 825, 5, doi: [10.3847/0004-637X/825/1/5](https://doi.org/10.3847/0004-637X/825/1/5)
- Spera, M., Mapelli, M., Giacobbo, N., et al. 2019, *MNRAS*, 485, 889, doi: [10.1093/mnras/stz359](https://doi.org/10.1093/mnras/stz359)
- Spurzem, R., & Kamlah, A. 2023, *Living Reviews in Computational Astrophysics*, 9, 3, doi: [10.1007/s41115-023-00018-w](https://doi.org/10.1007/s41115-023-00018-w)
- Stone, N. C., Küpper, A. H. W., & Ostriker, J. P. 2017, *MNRAS*, 467, 4180, doi: [10.1093/mnras/stx097](https://doi.org/10.1093/mnras/stx097)
- Strubbe, L. E., & Quataert, E. 2009, *MNRAS*, 400, 2070, doi: [10.1111/j.1365-2966.2009.15599.x](https://doi.org/10.1111/j.1365-2966.2009.15599.x)
- Takahashi, K. 1995, *PASJ*, 47, 561, doi: [10.48550/arXiv.astro-ph/9507040](https://doi.org/10.48550/arXiv.astro-ph/9507040)
- Tomczak, A. R., Quadri, R. F., Tran, K.-V. H., et al. 2014, *ApJ*, 783, 85, doi: [10.1088/0004-637X/783/2/85](https://doi.org/10.1088/0004-637X/783/2/85)
- Wang, L., Iwasawa, M., Nitadori, K., & Makino, J. 2020, *MNRAS*, 497, 536, doi: [10.1093/mnras/staa1915](https://doi.org/10.1093/mnras/staa1915)
- Wang, L., Spurzem, R., Aarseth, S., et al. 2015, *MNRAS*, 450, 4070, doi: [10.1093/mnras/stv817](https://doi.org/10.1093/mnras/stv817)
- Wang, L., Tanikawa, A., & Fujii, M. 2022, *MNRAS*, 515, 5106, doi: [10.1093/mnras/stac2043](https://doi.org/10.1093/mnras/stac2043)
- Woo, J.-H., Cho, H., Gallo, E., et al. 2019, *Nature Astronomy*, 3, 755, doi: [10.1038/s41550-019-0790-3](https://doi.org/10.1038/s41550-019-0790-3)
- Woosley, S. E. 2017, *ApJ*, 836, 244, doi: [10.3847/1538-4357/836/2/244](https://doi.org/10.3847/1538-4357/836/2/244)
- Woosley, S. E., & Heger, A. 2021, *ApJL*, 912, L31, doi: [10.3847/2041-8213/abf2c4](https://doi.org/10.3847/2041-8213/abf2c4)
- Yagi, K., & Seto, N. 2011, *PhRvD*, 83, 044011, doi: [10.1103/PhysRevD.83.044011](https://doi.org/10.1103/PhysRevD.83.044011)